Manuscript Details

Manuscript number JQSR_2019_634_R2

Title Landscape dynamics and human-environment interactions in the northern foothills of Cho Oyu and Mount Everest (southern Tibet) during the Late Pleistocene and Holocene

Article type Research Paper

Abstract

Here we present an integrated earth surface process and paleoenvironmental study from the Tingri graben and the archaeological site of Su-re, located on the southern rim of the Tibetan plateau, spanning the past ca. 30 ka. The study area is characterized by cold climate earth surface processes and aridity due to its altitude and location in the rain shadow of the Mount Everest–Cho Oyu massif and is thus sensitive to climatic and anthropogenic perturbations. In this highly dynamic geomorphic environment, paired-cosmogenic nuclide results from boulders on a massive hummocky moraine in the southern Tingri graben reveal complex exposure histories that limit our capability of directly dating the corresponding glacial advance, and shed a note of caution on previously published single-nuclide-based exposure ages along the northern Himalaya. Based on geomorphic considerations, however, the moraine clearly represents the local last glacial maximum, and likely coincided with a ~344±109 m depression of discontinuous permafrost zone relative to today during the global last glacial maximum (gLGM). This greatly intensified permafrost and periglacial hillslope processes and led to fluvial aggradation of the valley floors of ≥12 m. We observe formation of a thick (≥50 cm) pedo-complex starting at ca. 6.7 ka before present (BP) and erosional truncation at ca. 3.9 ka BP. Widespread landscape instability and erosion characterize the region subsequent to 3.9 ka and intensifies in the 15th century AD. Several lines of (geo)archaeological evidence, including the presence of pottery sherds, sling-shot projectiles and hammer stones within the sedimentary record, indicate human presence at Su-re since ca. 3.9 ka BP. Our data suggest that in the Su-re-Tingri area climatic conditions were warm and moist enough to allow vegetation expansion and soil formation only from ca. 6.7-3.9 ka, followed by weakening of the Indian summer monsoon (ISM) strength between ca. 4.2 and 3.9 ka, which is a prominent climatic event in the wider Asian monsoon region, and reflected in the investigation area by the 3.9 ka erosional boundary. Merging our Holocene landscape reconstruction with the geoarchaeological evidence, we speculate that the combined effect of Little Ice Age (LIA) cooling and an anthropogenic overuse of the landscape led to climatically induced landscape degradation and ultimately to an anthropogenically triggered ecological collapse in the 15th century. Such a scenario is in-line with regional historical data on declining monastery construction and migration of the ethnic group of the Sherpas. From an earth surface dynamics perspective, we find that transient landscape processes on the southern rim of the Tibetan plateau are strongly linked to millennial scale changes in the ISM intensity and duration. We identify three types of unidirectional non-linear ISM-landscape interactions. Given that the Tibetan plateau is the largest high-altitude landmass on our planet and our limited understanding of several of the key earth surface processes on the plateau, we pinpoint the need for more long-term (Quaternary scale) empirical data particularly on permafrost and periglacial processes and human-environment interactions

Keywords Tibet; monsoon; periglacial; permafrost; optical methods; cosmogenic isotopes; landscape degradation; Holocene; Pleistocene,

Corresponding Author Michael Meyer

Corresponding Author's Institution University Innsbruck

Order of Authors Michael Meyer, Luke Gliganic, Jan-Hendrik May, Silke Merchel, Georg Rugel, Frank Schlütz, Mark Aldenderfer, Karl Krainer

Suggested reviewers Jan Bloethe, Bernd Wuennemann, mark bateman, Adam Hudson, Lewis Owen

Highlights

- Depression of permafrost zone by ~450 m and ≥12 m of fluvial aggradation during LGM
- Favorable climate from 6.7-3.9 ka: formation of pedo-complex, truncated by mega drought
- LIA cooling & human impact causing ecological collapse during 15^{th} century AD?
- Three distinct types of interactions between monsoon and landscape processes identified
- Need for more research into periglacial processes and human-environment interrelations

Landscape dynamics and human-environment interactions in the northern foothills of Cho Oyu and Mount Everest (southern Tibet) during the Late Pleistocene and Holocene

Meyer, M. C. [1*]**; Gliganic, L. A.**[1]**; May, J-H.**[2,3]**; Merchel, S.**[4]**; Rugel, G.** [4]**; Schlütz, F.**[5]**; Aldenderfer, M. S.**[6]**; Krainer, K.** [1]

[1] *Institute for Geology, University of Innsbruck, Innrain 52, 6020 Innsbruck, Austria*
[2] *School of Geography, University of Melbourne, Carlton, VIC 3053, Australia*
[3] *Institute of Earth and Environmental Sciences, University of Freiburg, 79104 Freiburg, Germany*
[4] *Helmholtz-Zentrum Dresden-Rossendorf, D-01328 Dresden, Germany*
[5] *Lower Saxony Institute for Historical Coastal Research, D-26382 Wilhelmshaven, Germany.*
[6] *School of Social Sciences, Humanities, and Arts, University of California, Merced, CA 95343, USA.*

*corresponding author

Abstract

Here we present an integrated earth surface process and paleoenvironmental study from the Tingri graben and the archaeological site of Su-re, located on the southern rim of the Tibetan plateau, spanning the past ca. 30 ka. The study area is characterized by cold climate earth surface processes and aridity due to its altitude and location in the rain shadow of the Mount Everest–Cho Oyu massif and is thus sensitive to climatic and anthropogenic perturbations. In this highly dynamic geomorphic environment, paired-cosmogenic nuclide results from boulders on a massive hummocky moraine in the southern Tingri graben reveal complex exposure histories that limit our capability of directly dating the corresponding glacial advance, and shed a note of caution on previously published single-nuclide-based exposure ages along the northern Himalaya. Based on geomorphic considerations, however, the moraine clearly represents the local last glacial maximum, and likely coincided with a ~344±109 m drepression of discontinuous permafrost zone relative to today during the global last glacial maximum (gLGM). This greatly intensified permafrost and periglacial hillslope processes and led to fluvial aggradation of the valley floors of ≥12 m. We observe formation of a thick (≥50 cm) pedo-complex starting at ca. 6.7 ka before present (BP) and erosional truncation at ca. 3.9 ka BP. Widespread landscape instability and erosion characterize the region subsequent to 3.9 ka and intensifies in the 15th century AD. Several lines of (geo)archaeological evidence, including the presence of pottery sherds, sling-shot projectiles and hammer stones within the sedimentary record, indicate human presence at Su-re since ca. 3.9 ka BP. Our data suggest that in the Su-re-Tingri area climatic conditions were warm and moist enough to allow vegetation expansion and soil formation only from ca. 6.7-3.9 ka, followed by weakening of the Indian summer monsoon (ISM) strength between ca. 4.2 and 3.9 ka, which is a prominent climatic event in the wider Asian monsoon region, and reflected in the investigation area by the 3.9 ka erosional boundary. Merging our Holocene landscape reconstruction with the geoarchaeological evidence, we speculate that the combined effect of Little Ice Age (LIA) cooling and an anthropogenic overuse of the landscape led to climatically induced landscape degradation and ultimately to an anthropogenically triggered ecological collapse

in the 15th century. Such a scenario is in-line with regional historical data on declining monastery construction and migration of the ethnic group of the Sherpas.

From an earth surface dynamics perspective, we find that transient landscape processes on the southern rim of the Tibetan plateau are strongly linked to millennial scale changes in the ISM intensity and duration. We identify three types of unidirectional non-linear ISM-landscape interactions. Given that the Tibetan plateau is the largest high-altitude landmass on our planet and our limited understanding of several of the key earth surface processes on the plateau, we pinpoint the need for more long-term (Quaternary scale) empirical data particularly on permafrost and periglacial processes and human-environment interactions.

1. Introduction

With average elevation of ≥4500 m above sea level (asl), the Tibetan plateau (TP) and adjacent mountain ranges cover an area of approximately 2.4 Mio km^2 and thus form the highest and largest contiguous landmass on our planet. The Himalaya acts as the prominent topographic barrier and as an ecological transitional zone between the cool and arid TP and the sub-tropical Indian lowlands in the south and also hosts several of the highest mountain peaks in the world. As such the Himalaya hinders an effective moisture transport from the Indian Ocean onto the plateau, but also impedes human migration between India and Tibet (e.g. Bookhagen and Burbank, 2006; Aldenderfer, 2011). The moisture that does arrive on the plateau mainly originates from the Indian Summer Monsoon (ISM), particularly in the south and southeastern sectors of the TP (200-800 mm mean annual precipitation, ~90 % related to ISM), while the north and northeastern sectors of the TP typically receive significantly less than 200 mm mean annual precipitation and are under a stronger influence of the westerlies (Xu et al., 2008; Qi et al., 2016). The high elevation setting of the TP also entails low mean annual air temperatures (< ~10°C to well below 0°C; Xu et al., 2008; You et al., 2010) and favors the occurrences of extensive permafrost (Wang and French, 1995b; Cheng and Wu, 2007). These physio-geographic and climatic parameters in combination with the low effective oxygen levels on the TP (40-50% less on the plateau compared to sea level) put severe constraints on any living organism, including humans (Aldenderfer, 2011; Meyer et al., 2017). Vast stretches of the TP are thus best described as a high-altitude arid steppe and only the southern and eastern rim of the plateau holds grasslands that can support populations of nomadic herdsmen due to the influence of the ISM.

On the TP as well as in the Himalaya the ISM exerts a strong influence on earth surface processes and landscape dynamics via a range of geological and biological feedback mechanisms. As the single most important moisture source the ISM is also central for the socio-economic development of past and present societies in this region. The Late Pleistocene and the Holocene have seen dramatic fluctuations in both monsoon intensity and temperature on millennial to centennial timescales (e.g. Wang et al., 2008; Cai et al., 2012; Zhu et al., 2015; Kathayat et al., 2016). Given that large parts of the TP are situated at or beyond the current northern limit of the ISM and because of the high altitude and low mean annual air temperature on the TP, any swings in either precipitation or temperature must have had major effects on the landscape, ecosystems and high-altitude inhabitants. Reconstructing the climatic and paleoenvironmental evolution and associated landscape dynamics that played out on the TP under these varying precipitation and temperature regimes is thus important in order to understand (i) the present state of these high-altitude landscapes and ecosystems, and (ii) anticipate their potential future evolution. A solid understanding of terrestrial processes and their linkage to climate drivers is also mandatory for (iii) investigating possible linkages between climate, environment and the socio-economic development of historic and pre-historic Tibetan societies (Sinah et al., 2011; Kathayat et al., 2017).

Currently our understanding of the climatic history and environmental processes that operate on the TP is mainly based on Holocene lake sediments (e.g. Morrill et al., 2003; Bird et al., 2014; Conroy et al., 2017; Hudson et al., 2015; Shi et al., 2017), a limited number of speleothems (Cai et al., 2010; Cai et al., 2012), and several short and discontinuous aeolian records (e.g. Stauch, 2015). On the TP terrestrial archives that extend into the Late Pleistocene are rare (e.g. Zhu et al., 2015; Cai et al., 2010) as are studies about paleoenvironmental and paleoclimatic change from a multiple earth surface processes perspective on the scales of landscapes (e.g. Yan et al., 2018).

In this study we aim at furthering our understanding of the dynamic interactions between different earth surface processes and climate and consider the role of humans as geomorphological agents on the TP. We present the results of reconstructing landscape evolution and paleoenvironments in the southern TP over the past ca. 30 ka. We investigated a wide range of terrestrial archives and landscape features in the vicinity of an archeological site known as Su-re, situated in the northern foothills of Cho Oyu and Mount Everest. For chronology building luminescence and radiocarbon dating as well as cosmogenic radionuclide dating are used and sedimentological, geomorphological, geoarchaeological and pollen analysis are applied to a variety of sediments and geomorphic settings. This synoptic approach allows us to elucidate the complex landscape history and its potential climatic forcings, and is unprecedented in detail for this part of the TP. Integrating our landscape reconstruction with archaeological data also sheds new light on the potentially significant interactions between humans, landscape degradation and soil deflation.

2. Investigation area

The investigation area is situated north of the Mount Everest–Cho Oyu massif in southern Tibet within the Tingri graben. The north-south striking Tingri graben is the southernmost portion of the Tangra-Yum Co rift graben system that extends from the north face of Cho Oyu (8201 m asl) into the interior of the TP and formed in response to east-west extension during the Quaternary (Fig. 1a; Armijo et al., 1986; Taylor et al., 2003; Jessup and Cottle, 2010). Glacier-fed rivers originating from the Lapchi Range and the north side of the Cho Oyu massif are mainly responsible for the Quaternary infill of the Tingri graben and form an alluvial plain that is up to 15 km wide (Fig. 1b). Several hot springs and associated travertine deposits are bound to the active high-angle normal faults of the Tingri graben (Armijo et al., 1986; Hoke et al., 2000; Newell et al., 2008). The graben also cross-cuts the South Tibetan detachment system, i.e. a series of east-west striking low-angle normal faults with top-to-the-north-displacement (Fig. 1b; Burchfield et al., 1992). The South Tibetan detachment system juxtaposes high-grade gneisses, migmatites and leucogranites of the Greater Himalayan series with un-metamorphosed sediments of the Tibetan Sedimentary Sequence that are – in the Tingri area – Paleozoic to Cenozoic in age and consisting of Late Triassic (partly fossil bearing) sand- and siltstones, (occasionally bioclastic) limestones and shales (Burchfiel et al., 1992; Zhang, 2012; Jiang et al., 2016). The Tingri graben is filled with sediments mainly derived from reworking of the Tibetan Sedimentary Sequence (Armijo et al., 1986; Zhang, 2012).

Many of our sedimentological and geomorphological field investigations were focusing at and around the archaeological site of Su-re (or Shire; 4450 m asl), which is located on a south facing hillside on the eastern shoulder of the Tingri graben, ~10 km south-east of the Tibetan village of Lao-Tingri and ~45 km north of Cho Oyu (8201 m asl) and the Chinese-Nepali border (Fig. 1b). Su-re is a quartzitic sandstone lithic quarry and artefact scatter site (Gliganic et al., 2019). The surface artefacts are made of core and simple flake tools and were provisionally assigned to the Paleolithic based on typological analysis and comparisons with distant sites beyond the TP (Zhang Shenshui, 1976; Weiwen, 1994; Aldenderfer and Yinong, 2004). Coming from Lao-Tingri, Su-re also lies on the way to the Rongbuk valley and Monastery (4980 m asl) and the Everest base camp (5364 m asl, ~80 km driving distance). About 50 km south of Su-re a 5806 m high and glaciated mountain pass – known as Nangpa La – connects the Tingri area with the Khumbu Himalaya of Nepal. A foot-trail over Nangpa La was the traditional trade and pilgrimage route that connected the local Tibetans and Sherpas of the Khumbu until 1950.

Field investigations were also carried out on one of two prominent moraine lobes that are present in the southern part of the Tingri graben and were deposited when the Cho Oyu glacier (originating from the northern flanks of the Cho Oyu and the western flanks of the Lapchi range, respectively) and the Lapchi glacier (originating from the east side of the Lapchi range) advanced into the graben floor (Fig. 1b). The modern snouts of the Lapchi and the Cho Oyu glaciers are located at altitudes of ~5260 m and ~5130 m asl, respectively. These two glaciers are also the source of the two main rivers (referred to as Cho Oyu and Lapchi River, respectively) that drain the Tingri graben.

Today, the mean annual air temperature at Tingri is ~3-4°C with 300-450 mm of mean annual precipitation (Xu et al., 2008; Qi et al., 2016). The modern equilibrium line altitude (ELA) in the region (i.e. for glaciers of the Cho Oyu – Everest massif flowing onto the TP) is situated between ~5800-6200 m asl (Ye et al., 2015; King et al., 2016) and was estimated to lie at 6200 m asl for the Rongbuk glacier draining the north flank of Mount Everest (Owen et al., 2009). In contrast, discontinuous permafrost conditions across the Tibetan Plateau have been reported to reach down to ~4200 m asl in the north and ~4800 m asl in the south of the plateau (Wang and French, 1995c, Zhou and Guo, 1982), but are likely subject to regional scale variations. No detailed data for permafrost conditions around Tingri is so far available.

3. Methods

The wider Su-re area up to the Cho Oyu glacier was investigated during two field seasons in 2014 and 2016 (Fig. 1b). Geomorphological field mapping was aided by remotely sensed imagery (Google Earth) and detailed sediment logs were drawn from selected natural outcrops and hand dug pits.

Radiocarbon dating was conducted at the accelerator mass spectrometry (AMS) facilities of the Poznan radiocarbon laboratory and at the University of Salento, Italy (CEDAD) on macroscopic charcoal pieces and organic-rich sediment samples (n = 5; Table 1). Prior to Acid-Base-Acid treatment macroscopic contaminants visible under the binocular were removed by hand-picking and for sample R5 modern rootlets were additionally floated off. Measurement procedures in the CEDAD and Poznan laboratories followed those described in D'Elia et al (2004) and Brock et al (2010), respectively.

Optically Stimulated Luminescence (OSL) dating was performed at the University of Innsbruck to determine the sediment burial age for 20 coarse-grained sediment samples (Huntley et al., 1985; Rhodes, 2011; Table 2). Samples were collected by hammering 4-5 cm diameter opaque tubes into cleaned and logged sedimentary sections. Quartz grains of 180-212 μm diameter were extracted from the sediment samples in the laboratory under dim red illumination using standard procedures (Wintle, 1997; Gliganic et al., 2015). Hydrochloric acid (32%) and hydrogen peroxide (50%) were used to remove carbonates and organics, respectively. Sodium polytungstate solutions with densities of 2.70 g/cm^3 and 2.62g/cm^3 were used to isolate quartz and feldspar grains from heavy minerals and quartz from feldspar grains, respectively. A hydrofluoric acid (40% for 40 min) etch was used to remove the external, alpha-dosed rind of the grains (Aitken, 1998) and contaminant feldspars. Finally, grains were rinsed in hydrochloric acid and sieved again to retain the target grain-size fraction. Grains were loaded into a Risø DA20 TL/OSL reader (Bøtter-Jensen et al., 2003) and were measured using a post-IR blue protocol to ensure the purity of quartz OSL signals. Aliquots were stimulated with the Blue LEDs (470±30 nm) following infrared (IR) (875 nm) stimulations. The OSL signal was measured using an Electron Tubes Ltd 9635 photomultiplier tube and the ultraviolet emissions were measured through 7.5 mm of Hoya U-340 filter. IR stimulations were performed for 40 s at 50°C, and blue stimulations were performed for 40 s at 125°C. Signals were integrated using an early-background subtraction approach (Cunningham and Wallinga, 2010) where the signal was summed between 0 and 0.8 s minus a background integrated between 0.8 and 2.72 s. Laboratory irradiations were given using a calibrated ^{90}Sr/^{90}Y beta source mounted on the Risø DA20 TL/OSL reader.

Multi-grain aliquots comprising ~500 grains (5-mm diameter masks) were measured and equivalent dose (De) values were determined using the single-aliquot regenerative dose (SAR) procedure (Murray and Wintle, 2000). SAR measurements included regenerative dose preheats (10 s) and test dose preheats (5 s) of 240°C and 220°C, respectively. The appropriateness of the SAR procedure was assessed using standard tests, including a recycling ratio test, recuperation test (Murray and Wintle, 2000), OSL-IR depletion ratio (Duller, 2003), and dose recovery tests (Roberts et al., 1999; Murray and Wintle, 2003). The Central Age Model (CAM; Galbraith et al., 1999; Galbraith and Roberts, 2012) was used to model De distributions and determine representative De values.

The total environmental dose rate for each sample was measured using standard techniques. The results of beta counting using a GM-25-5 beta counter (Bøtter-Jensen and Mejdahl, 1988) and thick-source alpha counting and the conversion factors of Guerin et al. (2011) were used to calculate beta and gamma dose rates. The cosmic-ray dose rate was calculated following Prescott and Hutton (1994) and an internal alpha dose rate of 0.03±0.01 Gy/ka was assumed.

The age of four pottery samples was determined by measuring the pIRIR290 signal of a polymineral fine grain extract from the center of pottery sherds found in sedimentary sections and on the surface (Table 3). After the outer 2 mm of each ceramic sherd was removed in the laboratory, the remaining sherd was gently crushed with a mortar and pestle and the fine grain size fraction (~4-12 μm) was isolated by Stokes settling. Aliquots comprising polymineral fine grains were measured using the same equipment as sedimentary OSL samples. After a preheat of 320°C (60 s) and an IR bleach (50°C for 200 s), the blue emission of the post-IR IRSL (290°C for 200 s) signal was measured through the blue filter pack. The signal derived from the first 3 s minus a background integrated over the final 10 s was used to determine De values by the SAR procedure. An IR bleach (325°C for 200 s) was administered following the measurement of the test dose in each SAR cycle.

The dose rate of pottery sherds includes an alpha, beta, and gamma contribution from the sherd itself (sherd internal dose rate), an external gamma contribution from the surrounding sediments, and a cosmic contribution. The sherd internal dose rates could not be measured individually due to the small amount of material. Instead, the remains of samples C23a and C23b were crushed together to recover enough material, and the alpha, beta, and gamma contributions from the sherd material were measured using GM-25-5 beta counting and thick-source alpha counting. This dose rate was then used for all sherds. The gamma component from sediment sample TIN12, which was collected from an analogous sedimentary context as the sherds, was used as the external gamma dose rate, and its contribution to the apparent sherd dose rate was calculated following Aitken (1985; appendix H). The cosmic dose rate was calculated following Prescott and Hutton (1994).

A total of five samples were taken in the field for surface exposure dating with cosmogenic radionuclides (CRN; Table 4). Samples were taken by extracting ~350 g of rock from the surfaces of glacial boulders on the Cho Oyu moraine. Sample processing following standard methods and bulk samples have been enriched in quartz by standard physical and chemical treatment (Brown et al., 1991). CRN dating was conducted at the AMS facilities of the Helmholtz-Zentrum Dresden–Rossendorf, Germany. For Be and Al separation from quartz-rich samples, ∼300 µg of an in-house ^{9}Be carrier ('Phena EA', 2246 ±11µg/g ^{9}Be, Merchel et al., 2013) was added to the pure quartz samples before dissolution. Two processing blanks were treated along the samples with the same amount of acids, ^{9}Be carrier and additionally 750-1000 µg commercial ^{27}Al carrier. We applied a modified version of the measurement protocol described in Merchel and Herpers (1999) to extract Be and Al. The ^{27}Al concentration in the samples was measured from a representative liquid aliquot (1-4%) after dissolution by Inductively Coupled Plasma Mass Spectrometry (ICP-MS).

Isotope ratios were measured by AMS at the DREAMS facility (Rugel et al., 2016). Be ratios were normalized to the in-house standard SMD-Be-12 with a ^{10}Be/^{9}Be ratio of $(1.704\pm0.030) \times 10^{-12}$ (Akhmadaliev et al., 2013), which has been cross-calibrated to the NIST SRM 4325 standard (^{10}Be/^{9}Be = $2.79\pm0.03 \times 10^{-11}$) (Nishiizumi et al., 2007). Al ratios were normalized to the in-house standard SMD-Al-11. It has a ^{26}Al/^{27}Al ratio of $(9.66\pm0.14) \times 10^{-12}$ (Rugel et al., 2016), which is traceable to three primary standards from a round-robin exercise (Merchel and Bremser, 2004). Model bedrock erosion rates and/or exposure ages were calculated using the CRONUS-Earth online calculators (version 2.3 – http://hess.ess.washington.edu; Balco et al., 2008) and are reported here using the time-independent Lal/Stone scaling scheme (Stone, 2000). Generally, higher uncertainties on the ^{26}Al concentrations result from an estimated 3% uncertainty on the ^{27}Al ICP-MS data. Blank corrections from the processing blanks are negligible, i.e. <1% for both nuclides and all samples, besides ^{26}Al in sample Oyu_126.

Three organic-rich sediment samples (P1, P5 and P6) were analyzed for palynomorphs. Before taking the samples ~10 cm of sediment was removed from the exposure to avoid contamination with modern pollen. From each sample 2-3 ml were prepared by standard methods (HCl, KOH, acetolysis, HF and ultrasonic sieving at 5 µm mesh size). The extracted material was spiked with a *Lycopodium* pill and analyzed in glycerin. The palynomorphs were routinely counted under 400 x magnifications until 1000 *Lycopodium* spores have been encountered.

For four sediment samples (identical to the OSL samples Tin 9, 12, 14 and 19; Fig. 4) heavy mineral analyses were conducted for provenance analysis. The samples were sieved to the 90-212 µm grain size fraction and treated with a sodium polytungstate solution with a density of 2.9 g/cm^3. The heavy minerals were mounted on glass slides, embedded in Canada balsam and on average 289 grains were counted per sample under a polarizing microscope (supplementary online material (SOM) 1).

4. Results

4.1 Geomorphology at Su-re

The Su-re catchment is ~73 km^2 in size, unglaciated and consists of three unnamed tributaries 4 to 14 km in length (Fig 1b). It is situated within the northern foothills of the Mount Everest–Cho Oyu massif. The tributaries form an alluvial floodplain ~4435 m in altitude immediately to the south of the archaeological site of Su-re. This floodplain merges with the Cho Oyu floodplain ~1.2 km to the west of Su-re (Fig. 2). Shallow groundwater is locally favoring the occurrence of small wetlands within this alluvial plain. The archaeological site of Su-re lies adjacent to such a wetland that is ~1 km^2 in size (Fig. 2).

Three fluvial terrace levels were mapped in Su-re (Fig. 2): the lowermost terrace (T1) lies 1 to 1.5 m above the modern floodplain, while the terraces T2 and T3 are situated approximately 10 and 12 m above the modern floodplain, respectively. A fourth terrace level only slightly higher than T3 can locally be discerned and has been grouped with T3. The archaeological surface finds (ASF) at Su-re occur on a gently inclined hillside adjacent and upslope of these fluvial terraces and the highest density of ASF occurs over an area of ~2 hectares between 4450 and 4460 m asl (Fig. 3).

Small gullies and dry valleys cut into the foothills around Su-re and form alluvial fans that are adjusted either to the modern floodplain or to one of the fluvial terrace levels (Figs. 2 and 3). A laterally discontinuous aeolian cover sheet that is typically several tens of centimeters thick and composed of yellowish sand and silt is covering hillslope toes, fluvial terraces and alluvial fans. This cover sheet is partly stabilized by sparse vegetation comprising tussocks and shows a high density of blowouts (Fig. 2 and 3).

The hillslopes north and east of Su-re are rectilinear debris mantled slopes with slope angles ranging from 20°to >30°, which turn slightly convex towards the crest (~6-9°) and concave at the toe (~15-20°; Fig. 2). They are up to 4800 m asl in altitude, reveal smooth crests and are composed of shale and fine-grained sandstone as well as (bioclastic) limestone. Unsorted stripes starting at the hill crests and oriented parallel to the slope gradient occur. Along some north facing hillslope toes solifluction lobes can be observed (Fig. 2). Rock glaciers are relatively abundant in the northern foothills of Mount Everest, partly because of the softness and well developed schistosity of the host rock (i.e. Tibetan Sedimentary Sequence) resulting in thick talus deposits due to frost cracking which in turn are prone to rock glacier formation. On Google Earth imagery several dozen of such talus-derived rock glaciers were identified in the wider Su-re area that can be grouped into rock glaciers that are probably intact (containing ice) and relict (not containing ice) based on morphological criteria such as steepness of the front, surface flow structures, soil and vegetation cover (e.g. Barsch, 1996; Jones et al., 2018; Blöthe et al., 2019). Although a detailed rock glacier inventory has not been established in the course of this study, the altitude range covered by this random sample of rock glaciers that make up these two groups ranges from 5471 - 4870 m asl (median 4963±164 m; n = 12) for the intact and from 4808 – 4450 m asl (median 4578±141 m; n = 6) for relict rock glaciers, respectively (SOM 2).

4.2 Sedimentary record at Su-re

About 20 sediment outcrops or pits were investigated and sampled for ^{14}C and OSL dating and their locations are indicated in Figure 2 and 3, respectively. For the most representative of these (n = 16), detailed sediment logs are shown in Figure 4. These sediment logs come from (i) along two gullies that are situated directly south and southeast of the ASF area (log G-1A to G-2B), (ii) two pits dug at the hillslope toe within the ASF area (log pit-H1 and H2), (iii) along a gully that incises into an inactive alluvial fan ~450 m east of the ASF area (log F-1 to F-A2), (iv) from a tributary valley ~1 km northwest of the ASF area (logs Tv-1 to Tv-3), (v) from fluvial terrace sediments along the modern river bed (log R-1 to R-4), and (vi) from a blow-out(log Bo-180; Fig. 5d). Sediments exposed are generally coarse-grained (i.e. sand-sized or coarser) and encompass a range of colours and sedimentary properties, allowing their classification into five main sedimentary lithofacies, as well as the distinction of pedogenic horizons and processes (Fig. 4):

Lithofacies A: Coarse-grained, organic-free, clast-supported and often stratified gravels (facies A1) of light brownish colour characterize the basal sections of logs along the T1 river terrace. There are occasional gravelly sand lenses of up to 10 cm thickness. In general, the gravels are moderately to poorly sorted, show sub-rounded to angular clast morphologies and rare b-axis imbrication. In logs R-1 and R-4 these sediments are directly overlain by clast-supported but well-sorted and often imbricated gravels (facies A2). Based on these characteristics, lithofacies A likely indicate deposition in a fluvial channel environment with facies A2 reflecting transport by a more perennial stream with increased potential for sorting and rounding of clasts.

Lithofacies B: While in logs R-1 and R-4 lithofacies A represent the upper 60-80 cm of the logs, diamictic and very poorly sorted sediment composed of matrix-supported gravel characterize the upper part of the sections in logs R-2 and R-3 (Fig. 5a). Clasts within such diamictic sediments are angular and up to 40 cm in diameter. The diamict in log R-2 also contains cm to dm-sized sherds of red pottery (Figs. 5b and SOM 3). Based on these characteristics and the geomorphic setting downstream of a gully just ~300 m and 600 m to the northwest (Fig. 2), lithofacies B is interpreted as alluvial deposits originating from debris-flows or hyper-concentrated flow events derived from local hillslopes or gully systems. Lithofacies B also forms a dominant part of the logs situated in the adjacent tributary valley (Tv-1 and T-2) that is clearly set in an alluvial fan context.

Lithofacies C: In logs R-1 and R-3 the fluvial and alluvial sediments are overlain by markedly light grey to whitish, organic-free sandy mud and massive gravelly sands with only occasional faint stratification. While along the river terraces (R-1 to R-4) these sediments contain negligible amounts of pebble-sized clasts (facies C1-3), these strikingly pale-coloured and organic-free sediments also occur in depths ≥80 cm in most other logs in hillslope settings around the wider ASF area. However, here they are notably coarser (pebbly to cobbly sand) and contain varying amounts of angular clasts of up to ~10 cm in size (facies C4; log G-1B to G-2B, Pit-H, F-1 to F-A2; Fig. 4). Given the increasing grain size with proximity to the hillslope and the marked whitish colour we interpret these sediments as periglacial cover deposits resulting from (i) permafrost related solifluction and soil creep. Underlying continuous permafrost would also (ii) lead to moisture-saturated and reducing conditions within the deposit during the transport and helps explaining the markedly whitish colour inherent to these deposits in hillslope and terrace settings. In addition, these periglacial sediments often exhibit a gradual but highly irregular and distorted lower boundary where they grade into more yellowish-brownish sediments of otherwise similar properties, possibly reflecting the spatial coincidence of sediment movement and a sharp hydrological and soil chemical gradient across the lower boundary of a seasonally thawed surface layer above permafrost (i.e. active layer). Further evidence for periglacial conditions associated with these sediments is provided by a wedge-shaped feature filled by periglacial sediments (log G-1A) as well as highly convoluted stratification and upper boundary with overlying fluvial sediment in log R-1 that are together indicative of freeze-and-thaw related processes leading to cryoturbation.

Lithofacies D: In their upper parts, most logs in the ASF area as well as the log Tv-3 are characterized by yellowish cross-bedded sand typically 20-100 cm thick with intermittent stonelines, i.e. thin accumulations of clasts in otherwise clast-free sands (log Pit-H, F-1 to F-A2; Figs. 4 and 6d). Provided the spatially extensive occurrence of these sediments and clear geomorphic association with wind generated blowouts (e.g. Bo-180) these sediments are reflecting deposition by aeolian processes.

Lithofacies E: In the gully outcrops G-1A to G-2B the upper parts of the section are built from finely stratified layered yellowish gravelly sand with varying amounts of cm-sized angular clasts within the sandy matrix. Given their cm-scale stratification and poor sorting in a gully and alluvial fan context, these sediments likely represent hillslope deposits laid down by water in a non-channelized environment, e.g. slopewash or minor sheet-flood events with only local-scale run-off and sediment transport.

While overall sediments in the documented logs are characterized by pale whitish, yellowish or grey-brownish colours, most logs also exhibit horizons that are (i) ~20-50 cm in thickness, have a slightly loamy texture and are reddish to brownish in colour; and (ii) ~10-30 cm in thickness, wavy and laterally discontinuous but are distinctly blackish in colour (Fig. 5c). Both of these horizons generally have gradual lower boundaries and are interpreted as pedogenic horizons with the former likely representing a Bv horizon formed from in-situ weathering, oxidation and minor rubefication, and the latter indicating the presence of organic-rich (logs G-1B to G-2B) and even peaty (e.g. log F-1) horizons mostly associated with depressions and topographic lows (e.g. along gullies; Fig. 2). In log G-1A an even older paleosol that has been identified at the base of the log exposing a very reddish and clay-rich horizon with carbonate nodules that have not been observed in any other log. Where not buried by aeolian or slope sediments, the Bv horizon has almost exclusively formed in periglacial sediments (Fig. 5c). The lower contact of the Bv horizon with periglacial slope sediments is partly characterized by a sharp erosional boundary (e.g. Pit-H) but often also grades into an underlying organic horizon (e.g. logs G-1A, G-2B, F-1). In contrast, the upper contact between the Bv horizon and the aeolian cover sediments and/or slopewash sediments along the gully (logs G-1A to 2B) is always represented by a sharp erosional boundary and in the former case associated with the occurrence of stonelines (Fig. 4).

From the sediment logs G-1A and F-1, three organic-rich sediment samples were analyzed for palynomorphs (P1, P5, P6; Fig. 4). The concentration of pollen or other organic microfossils was low due to strongly oxidizing conditions in the sampled sediments and paleosols and only spores of the Glomus type were encountered in higher concentrations in all three samples (31, 79 and 123 counts for sample P1, P5 and P6, respectively). The other palynomorphs in these samples included Picea pollen fragments (n=2), a conifer-tracheid with piceoid pits (n=1), a monolete fern spore (n=1), a spore of the Riccia-type (n=1), Arcella shells (n=4) and 2 charred pieces of grass epidermis.

Because oxidation is strongly counteracting pollen preservation the absolute pollen concentration in our samples is low. Yet, we exclude far-distance pollen transport e.g. via advection from south of the High Himalaya because (i) it is extremely unlikely that all the regional and local pollen (that were certainly present in higher abundance in the original sediment) were oxidized and only the far-distant-transported pollen were preserved; (ii) wind transport of spores of the ground-living lever-moss Riccia and shells of Arcella is very unlikely; and because (iii) local occurrence of conifers is especially underlined by the findings of tracheids from conifer wood. This interpretation is supported by the fact that the Glomus type spores, which are resistant to oxidation, are the most abundant ones in all our samples. Hence, while our pollen data are not allowing for any quantitative palynological inferences, they certainly provide a qualitative paleoecological snapshot reflecting aspects of the local to regional vegetation as discussed below.

From a lithological point of view almost all clasts encountered in the Su-re sediment sections (Fig. 4) are from the Tibetan Sedimentary sequence (shales, fine-grained sandstones and siltstones), originating from the local hillslopes or the Su-re tributaries 1 to 3 (Fig. 2). The vast majority of these un-metamorphosed clasts reveal angular to sub-angular clast morphology and only few clasts from the fluvial sediment logs are sub- to well-rounded. However, migmatites and leucogranites from the Greater Himalayan series typically well-rounded, spherical in shape and with an average diameter of ~6 cm occur too (Table 4; Figs. 3, 6e and f). Such clasts have only been observed at or close to the ground surface, i.e. atop or within the aeolian cover sheet or atop the Bv horizon. Furthermore, heavy mineral analysis conducted on aeolian (TIN 12 and 19), periglacial (TIN 9) and fluvial (TIN 14) sediment samples reveal very similar mineral assemblages (SOM 1) for all samples, suggestive of a single local source area, regardless of sediment type or sediment transport mechanism.

4.3 Geomorphology and sedimentology of Cho Oyu and Lapchi moraine lobes

About 13 km south of Su-re a prominent and up to 4 km wide moraine lobe was deposited by the Cho Oyu paleoglacier. The lobe represents a massive hummocky moraine reaching down to an altitude of 4653 m asl and extending as a continuous moraine blanket for ~7 km up valley. For the initial 2.8 km the surface morphology of this hummocky moraine is irregular, while from 2.8 to 7 km transverse ridges become more and more common (Fig. 6a). Individual hummocks and kettle holes range between 10 and 150 m in diameter. A contorted ridge with a height of ~10-15 m relative to the glacier forefield outlines the hummocky lobe and the highest part of the lobe is made up by individual transverse ridges (Fig. 6b). A distinct latero-frontal moraine is missing. Further up-valley this contorted moraine ridge merges into a lateral moraine that can be traced for ca. 15-16 km to altitudes of ~5400 m asl.

The sedimentary facies of the hummocky moraine is sandy boulder-gravel. Decimeter sized sub-rounded to angular clasts are embedded in a sandy matrix. Individual boulders are up to several meters in diameter. The boulders and clasts are migmatites and leucogranites from the Greater Himalayan series. In depressions and kettle holes sand has accumulated, smoothing the surface topography of the moraine. No standing water was observed on the hummocky lobe surfaces. Where the sediment facies of the hummocky moraine is sandy a thin soil has developed. This soil is characterized by a 20-30 cm thick slightly reddish to brownish Bv horizon where preserved from ongoing surface erosion. The hummocky moraine and its outer ridges are sparsely vegetated with grass.

1.2 km to the west the Lapchi moraine lobe reveals a geomorphological and sedimentological picture very similar to the Cho Oyu moraine lobe. The Lapchi lobe is up to 4.8 km wide and also composed of a massive hummocky moraine that lacks a distinct latero-frontal moraine but reveals a semi-continuous transition into the glacier fore field. No evidence for more extensive glacial advances beyond the Cho Oyu and Lapchi moraine lobes to altitudes below 4600 m asl has been observed.

The Cho Oyu and Lapchi Rivers have incised up to 40 m into these hummocky moraines and left a set of fluvial erosional terraces, of which the most prominent ones are indicated in Figure 6a (terrace 1, 2 and 3, situated ~13, 25 and 36 m above the modern river channel). Numerous supra-glacial paleo-meltwater channels radiate from the hummocky moraines outward into the paleo-glacier fore field forming a dense network of braided channels that can be traced from the moraine lobes for 4 to 5 km down valley before becoming covered by younger aeolian sand. A thin (10-20 cm) brownish to reddish soil has developed on this glacial outwash plain and the modern Cho Oyu and Lapchi Rivers are currently cutting into this plain.

4.5 Radiocarbon and luminescence chronology

Six samples were submitted for radiocarbon dating of which five yielded sufficient carbon after ABA treatment and combustion for subsequent AMS measurement (Table 1). For sample R6 the carbon yield was very low (<1%) and the radiocarbon age is therefore deemed unreliable. Sample R5x is a replicate sample of sample R5, and the latter has (in addition to hand picking of macroscopic contaminants) also seen floatation treatment in order to remove tiny rootlets that might go undetected via a hand picking approach. The age discrepancy of ca. 2.3 ka between both samples is likely to result from these different pre-treatment steps and suggests that modern rootlet contamination was not completely removed from sample R5x. Hence, sample R6 and R5x are omitted from the stratigraphic logs in Figure 4.

Nineteen sediment samples were collected for OSL dating from logged outcrops at Su-re (Figure 4). A typical OSL decay curve and dose-response curve are shown in Fig. 7. Dose recovery results for 31 aliquots from samples Tin3, 5, 6, 9, 10, and 11 yield measured/given dose ratios consistent with unity (1.08±0.04) with recycling ratios of 1.00±0.03, recuperation values of

1.25±0.17%. These results indicate that the SAR procedure can accurately estimate known radiation doses for samples from Su-re.

Equivalent dose, dose rate, and age data for OSL samples are shown in Table 2. Overdispersion values range from 0 to 48% (20±6% on average). Given the generally low overdispersion values and consistent radial plots (Fig.7) for multi-grain aliquot De data, the ages for most samples were calculated using De values determined using the CAM (Galbraith et al., 1999; Galbraith and Roberts, 2012). However the data for two samples suggest that this approach may not appropriately yield an accurate depositional age. The two samples with the highest overdispersion values (i.e., TIN13 and TIN4y) have De distributions with two apparent populations of grains (Fig.7) and yield CAM ages that are stratigraphically inconsistent. However, when a weighted mean is calculated for each population in these two samples using the CAM (Table 2), the resulting ages that are based on the main De population are stratigraphically coherent. Neither the form of the De distributions nor the sediment transport mechanism for these samples (both are of aeolian origin) make partial bleaching a likely explanation for the observed De outliers and we thus suggest post-depositional mixing of older and younger sedimentary units as the more plausible explanation. For sample TIN13 the high De component comprises two aliquots only and we suppose that intrusive high-De grains from the deeper Pleistocene cryoturbated deposits are the underlying reason for these outliers. Sample TIN4y was obtained from 40 cm depth in log F-1, where modern rootlets were frequently observed. Modern rootlet contamination was also identified as the cause for age underestimation of the adjacent radiocarbon sample R5X. We thus suspect that modern grains were mixed into the underlying Bv horizon from where OSL sample 4y was obtained, hence that the high De component is representing the burial event and was consequently used for age calculation.

Table 3 shows equivalent dose, dose rate, and age data for pIRIR290 data from four pottery sherds. Three of these ceramics (C22, C23a, and C23b) were collected from an outcrop along the river, ~40 cm below the surface (log R-2; Fig. 2 and 4), while C28 was collected from the surface of terrace 2 ~64 m northwest of log R-3 (Fig. 2).

Dose recovery and residual measurements were performed; following a 600°C bleach (the approximate temperature of pottery firing) half the aliquots were measured, yielding a residual consistent with zero. The other half of the aliquots were given a 3.9 Gy surrogate natural dose and were then measured using the pIRIR290 SAR procedure. Measured/given dose ratios consistent with unity indicate the measurement protocol can accurately estimate known doses. De values were measured for between four and 12 aliquots for each sample, which yield ages of 0.86±0.05 ka (TIN22), 0.73±0.05 ka (TIN23a), 0.78±0.05 ka (TIN23b), and 0.50±0.05 ka (TIN28).

4.6 Cosmogenic radionuclide concentrations

The AMS-measured ^{10}Be concentrations in all five samples from glacial boulders range between ~0.8 to 1.7 x 10^6 atoms/g while ^{26}Al concentrations range from 1.9 to 7.6 x 10^6 atoms/g (Table 4). The resulting calculated zero-erosion surface exposure ages vary between 11.8±1.3 ka and 26.7±2.4 ka based on ^{10}Be concentrations, and between 4.9±0.6 ka and 19.2±1.8 ka for ^{26}Al concentrations (Table 4).

5. Discussion

5.1 Late Pleistocene permafrost and (peri)glacial activity and concomitant valley floor evolution

The debris covered slopes in the Su-re area show clear evidence for slow mass wasting processes under both, periglacial and/or permafrost conditions, including solifluction lobes, striped slopes, rectilinear slope morphologies and rock glaciers. Periglacial differ from permafrost processes in as far as both being frost related processes, the latter involving either sporadic, discontinuously or continuously frozen ground conditions all year round (French and Thorn, 2006). Solifluction lobes and striped slopes are commonly interpreted as a periglacial creep phenomenon (Matsuoka et al., 1997; French, 2007; French and Bjornson, 2008). Field observations and satellite imagery support the interpretation of striped slopes at Su-re as a periglacial creep phenomenon. We observe a spatial relationship between stripes and outcrops of colored host rock, suggesting that striped slopes result from sliding of debris originating from in-situ weathering of differently colored host rock in up-slope positions (Jahn, 1985; Church et al., 1979; Matsuoka et al., 1997). At the other hand, debris covered rectilinear slopes and talus-derived rock glaciers (i.e. perennially frozen and ice-rich debris on non-glacierised mountain slopes) develop under permafrost conditions only (e.g. Jahn, 1985; Iwata, 1987; French, 2007; Haeberli et al., 2006). Our field and remote sensing observations show that in the northern foothills of the Mount Everest-Cho Oyu massive rectilinear slopes and talus-derived rock glaciers are ubiquitous, and that the rock glacier fronts from the Su-re area range in altitude from ~5470 – 4450 m asl. (SOM 2).

Published palaeoclimatic data from High Asia allow us to gain deeper insights into the modern versus Late Pleistocene permafrost dynamics on the TP, relevant for understanding the morphodynamics at Su-re. Permafrost research in High Asia suggests that the current lower limit for discontinuous permafrost is broadly situated at ~4980 m in the Nepalese Himalaya (i.e. adjacent to Su-re; Ishikawa et al., 2001; Jones et al., 2018) and at ~4800 m asl. in the south-central part of the TP (Wang and French, 1995b, Zhou and Guo, 1982). For mountain ranges in continental climate settings (including the Alps, the Himalaya, Karakoram, Tien Shan and Tibet) it has been demonstrated that the lower limit of discontinuous permafrost broadly coincides with the ~-2°C isotherm for mean annual air temperature (Haeberli, 1983; Shi and Li, 1989; Barsch, 1992; Ishikawa et al., 2001; Mitchell and Taylor, 2001; Blöthe et al., 2019). In other words, at Su-re the ~-2°C isotherm and thus the lower limit of discontinuous permafrost and thus intact rock glacier fronts should roughly lie at ~4800 - 4980 m asl. Various authors have estimated that the mean annual air temperature for the TP was ~-2°C lower during the LGM compared to today (Kirchner et al., 2011; Heyman et al., 2014) and about 2.8°C lower in the Shisha Pangma area (~80 km west of Su-re; Schäfer et al., 2008). Using an adiabatic lapse rate of ~0.85°C/100 m (calculated for southern Tibet; Kattel et al., 2015) or 0.62°C/100 m (derived for the Shisha Pangma area; Schäfer et al., 2008) results in a depression of the discontinuous permafrost zone by ~235 – 452 m (344±109 m) during the LGM compared to today. The lowest and highest absolute estimates for discontinuous permafrost occurrences and by implication rock glacier activity during the LGM in the Su-re area thus range from ~4456 – 4745 m asl. Such a depression of the permafrost zone would be sufficient to almost establish discontinuous permafrost conditions in the floodplain of Su-re (at 4435 m asl.), and would certainly greatly enhance permafrost and periglacial processes on the hillslopes above Su-re on a catchment scale.

The rock glaciers that have been mapped in the course of this study (SOM 2), broadly support these estimates of altitudinal shifts of the permafrost zone: the group of intact rock glaciers with a median altitude of 4963±164 m coincides with modern permafrost estimates of Wang and French (1995b), Zhou and Guo (1982) or Jones et al. (2018). The group of relict rock glaciers (median altitude 4578±141 m) falls within the calculated range of discontinuous permafrost depression for the LGM (i.e. 4470 – 4740 m asl). The underlying assumption is that the relict rock glaciers at Su-re can indeed be assigned to the LGM. A more complete rock glacier inventory and more robust age constraints of intact and relict rock glaciers are needed to substantiate such estimates and palaeoclimatic inferences. Nevertheless, these calculations highlight both, the magnitude and the potentially important role that shifts in permafrost zone might play for the landscape dynamics at Su-re.

OSL dating reveals that the Su-re sedimentary record covers the time interval since the latest Pleistocene. The OSL ages of 26.2±2 ka and 23.4±1.5 ka (pit-H1), and 26.6±1.7 ka and 18.4±1.0 ka (base of pit-H2) obtained on organic-free and solifluced sediments from a hillslope toe position indicate that periglacial and permafrost activity (cryoturbation, solifluction) was strong during the global Last Glacial Maximum (gLGM, Clark et al., 2009; Figs. 3, 4 and Table 2). Three of the four OSL ages overlap within uncertainties with the onset of gLGM (ca. 26 ka; Clark et al., 2009). Similarly, an ice wedge cast with an OSL age of 14.0±0.9 (log G-1A) as well as organic-free and cryoturbated sediments with OSL ages of 11.1±0.7 ka (log F-1), 10.9±0.8 ka (log Tv-1) and 11.1±0.7 ka (log R-1; Fig. 4 and Table 2) also suggest strong periglacial activity and permafrost occurrence subsequent to the gLGM, with a noticeable clustering of OSL ages just prior and at the very beginning of the Holocene.

The OSL age of sample TIN 14 suggests that the clast supported fluvial gravels along the river terrace outcrops (log R1 to 4) have been deposited ca. 25.7±1.6 ka ago (Fig. 4). The poor sorting and high percentage of sub-angular clasts in combination with the clast lithologies (all clasts are derived from the Tibetan Sedimentary sequence) imply short transport distances and local sediment sources from tributaries immediately upstream of the Su-re site. These sedimentary and geochronological data suggest enhanced solifluction and permafrost creep on the hillslopes around the Tingri graben up to an altitude of ca. 5500 m asl (i.e. the altitude of the local hillslope crests), and a resulting excess of coarse sediment in the river valleys early during the gLGM, which in turn forced local rivers to aggrade. This interpretation is in line with the OSL ages of 26.2±2 ka and 23.4±1.5 ka from pit-H1, and 26.6±1.7 ka from pit-H2 where organic-free and solifluced sediments at the hillslope toe at Su-re suggest strong periglacial activity at the onset of the gLGM (Fig. 3 and 4).

The Cho Oyu and Lapchi moraine lobes are both massive hummocky moraines with identical geomorphic and sedimentological characteristics, suggestive of a simultaneous advance of debris covered glaciers from the Cho Oyu and the Lapchi massifs (Benn and Owen, 2002; Benn et al., 2003). Both hummocky lobes lack a distinct latero-frontal moraine ridge, which we interpret as evidence for a single and short lived glacial advance. Paleo-meltwater channels that radiate out from these hummocky lobes merging into an ancient outwash plain support this interpretation. Further up-valley morphologically distinct lateral moraine ridges evolve from these hummocky lobes. From a geomorphological point of view, it appears that these lateral moraines and the hummocky moraine belong to a single advance representing the local last glacial maximum. Five boulders from the Cho Oyu hummocky moraine surface were sampled in our study and ^{10}Be based apparent CRN surface exposure ages range from ca. 12 to 27 ka while ^{26}Al based apparent CRN surface exposure ages range from ca. 5 to 19 ka (Table 4; Fig. 6). These ages seem to be in broad agreement with (i) previously published gLGM exposure ages of Chevalier et al. (2011) from CRN dated boulders (mean age of 25±2 ka, using scaling of Lifton (2005); no outliers identified) from the left lateral moraine that connects with the Cho Oyu hummocky moraine (Fig. 6), and (ii) a geomorphological model for hummocky moraine evolution based on 75 CRN dated boulders from the Pamir (Zech et al., 2005). However, these authors have only measured cosmogenic ^{10}Be in their samples, and thus cannot exclude the presence of complex exposure histories (Chevalier et al., 2011). Our concentrations from both ^{26}Al and ^{10}Be therefore – for the first time along the northern slopes of the Himalaya – provide an opportunity to test the assumption of simple, steady-state erosion scenarios for boulders on debris covered moraines coming down from the Himalaya. When combined, ^{10}Be concentrations and the $^{26}Al/^{10}Be$ in our five Cho Oyu samples in fact show significant deviation from the steady-state erosion line implying complex exposure histories with burial on the order of 1 Ma for sample Oyu-126 (‘banana plot’; SOM 4). In addition, sample Oyu-128 plots into a “forbidden” zone above the steady-state erosion line. In combination these results may either (i) hint to the presence of long-term burial and storage of glacial boulders in one of the most dynamic geomorphic environments in the world, or (ii) provide further evidence for the presence of erosional transience and time-varying erosion rates (Knudsen and Egholm 2018). The latter could be caused, e.g. due to the presence of accelerated erosion events such as deep plucking, extremely high uplift and exhumation rates, and/or temporally highly variable ice thicknesses. While all processes have a realistic potential for influencing geomorphic processes in the Cho Oyu valley, our results and considerations will benefit from further work and modelling, but serve here to shed a note of caution on exposure ages based on a single nuclide alone in the highly dynamic geomorphic environments of the Himalaya.

5.2 Morphodynamics during the Early to Mid-Holocene (11.7 to ca. 4 ka BP)

The sedimentary record suggests that during the onset of the Holocene the Su-re area continued to be devoid of any notable vegetation cover and experiencing intensive periglacial activity, as indicated by the OSL dated cryoturbated and organic-free sediments in log F-1 (11.1±0.7 ka), log R-1 (11.1±0.7 ka) and log Tv-1 (10.9±0.8 ka; Fig. 4), i.e. conditions akin to the gLGM. Mid-Holocene radiocarbon ages, clustering at ca. 6.4 ka cal. BP, were obtained from the blackish organic-rich horizons that stratigraphically follow above these organic-free periglacial deposits (Fig. 4 and 5c; Table 1). These organic horizons only occur in local depressions or along gullies, where water availability and soil moisture were probably enhanced, at least on a seasonal base. In terms of the palynomorph content, only *Glomus*-type spores were recovered in significant numbers from these organic-rich horizons (samples P1, P5, P6; Fig. 4). *Glomus*-type spores are produced by soil fungi that grow in symbiotic association with green plants and are much more resistant to decomposition compared to most other spore or pollen grains that decay (oxidize) rapidly in soils. The other palynomorphs extracted from these organic-rich horizons hint towards moist conditions (e.g.

presence of fern spores or *Arcella* - a genus of amoebae, typical in freshwaters and mosses, but rare in soils) and the presence of conifers (e.g. *Picea* pollen and conifer wood fragments). These geomorphological, sedimentological and palynological observations suggest that the organic-rich horizons partly derive from eroded soil material that has been washed into topographic lows, where locally moist conditions facilitated plant growth and organic (sometimes peat-like) material to accumulate. It is noted that the modern landscape at Su-re lacks any shrubs or tree stands, but that palynomorphs indicate the presence of *Picea* ca. 6.7 ka ago (samples P1 and P5).

A discontinuity of ca. 4 to 5 ka exists between deposition of the periglacial and organic-free deposits of the earliest Holocene and these organic sediments. The exact nature of this discontinuity at Su-re is currently unclear and might either (i) represent a prolonged period of non-deposition or (ii) result from erosion due to enhanced surface run-off in response to increased monsoon intensity during the early Holocene. Looking at the stratigraphic evidence (i.e. organic-rich sediment accumulation in topographic depressions starting not before 6.7 ka followed by pedogenesis) we favor interpretation (i). We thus hypothesize that the regional paleoenvironmental conditions turned warm and moist enough only during the Mid-Holocene, initiating widespread vegetation growth and soil formation on a probably up to that point still largely barren landscape.

Four OSL samples have been taken from the Bv horizon that developed stratigraphically above the organic-rich sediments and the corresponding optical ages range from 6.4±0.4 ka to 3.9±0.4 ka (Fig. 4 and 5c; Table 2). In each sediment log all OSL and radiocarbon ages are in stratigraphic order and the Bv horizon acts as a prominent marker horizon allowing for stratigraphic correlation across distant outcrops.

Further sedimentological and pedological observations can be made and are relevant for our interpretation of the Bv horizon at Su-re: The Bv horizon is sandy-silty and either completely devoid of large clasts (log G-1A, F-1, F-A1) or reveals a fining-upward trend and an overall significantly lower clast concentration compared to the underlying Pleistocene sediments (log G-1B, G-2A, G-2B, Pit-H, Tv-1 and 2; Fig. 4). It is also slightly calcified in some places. Pedogenic processes were thus not simply penetrating into the pre-existing (coarse-grained and unsorted) Pleistocene underground. In combination, our observations suggest that soil formation was taking place while sandy to silty sediment was gradually accumulating on the hillslopes of Su-re starting from ca. 6.7 ka onward. This is also reflected by our OSL samples in the Bv horizon that all come from slightly different stratigraphic positions within the up to 50 cm thick Bv horizon. The spread in the optical ages could thus be interpreted as evidence for continuous and likely cumulic pedogenesis throughout the middle Holocene (i.e. pedogenesis with contemporaneous accretion of sediment on the hillslopes over a timespan of ca. 2.5 ka).

An increase in moisture and development of a vegetation cover at that time likely facilitated (i) sheetwash processes by overland flow, and/or (ii) trapping of aeolian sand and silt that were constantly blowing out from the adjacent floodplains e.g. via katabatic winds. Accumulation and stabilization of aeolian sediments by vegetation and concomitant soil formation has been identified as an important mechanism in arid and semi-arid regions (e.g.Bateman et al., 2003; Leighton et al., 2014) and is also deemed relevant for the TP (Sun et al., 2007; Lu et al., 2011; Yu and Lai, 2014; Stauch, 2015). The Bv horizon is truncated by a sharp erosional boundary and an associated A horizon is not preserved in any of the sediment logs and was likely removed completely by erosion.

Furthermore, the reddish to brownish Bv horizons mapped on the Cho Oyu and Lapchi hummocky moraines and in the adjacent glacial outwash plain probably represent similar pedogenic processes and timing.

We thus suggest that an up to 50 cm thick pedo-complex evolved in the wider Su-re area in response to warmer and wetter climatic conditions from ca. 6.7 ka onward. Under these ameliorated climatic conditions an initial vegetation cover and associated A horizon (that has partly been eroded and deposited as organic-rich sediment horizons in local topographic depressions) formed that in turn facilitated trapping of aeolian sediment and furthered soil formation. Accumulation and stabilization of aeolian sediment via a relatively continuous vegetation cover continued during the Mid-Holocene under prevalent moist and warm climatic conditions until ca. 3.9 ka.

5.3 Morphodynamics during the Late Holocene (ca. 3.9 ka to 0.5 ka BP)

In the gully southwest of the ASF area (logs G-1A to G-2B; Fig. 4 and 5c) the Bv horizon is overlain by finely layered (mud flow-like?) slope wash deposits with an OSL age of 0.61±0.08 ka (Table 2). In the outcrops situated along the hillslope (logs pit-H1 and H2, F-1 to F-2A, Bo-180, Tv-2) an aeolian cover sheet, frequently revealing accumulation of coarse clasts (a basal stoneline?), follows above the Bv horizon blanketing most of the landscape at Su-re. Four OSL ages (samples 5, 6, 16 and 19; Fig. 4 and Table 2) constrain these aeolian sands to 0.55±0.08 ka (central weighted mean age and standard deviation). The OSL samples 5 and 6 are from the base and near-top of the sediment log Bo-180 (Fig. 5d), where the aeolian cover sheet attains a thickness of 1.8 m and the OSL ages overlap within uncertainties, indicating rapid rather than gradual accumulation of these windblown sediments. OSL dating of the slope wash and aeolian deposits thus suggests significant landscape instability in the very recent geological past, i.e. approximately during the 15th century anno domini (AD.).

A sharp erosional boundary separates these slope wash and aeolian deposits from the underlying Bv horizon. This erosional boundary occurs in all outcrops and suggests a sudden change from stable and/or depositional to erosional morphodynamics subsequent to the formation of the Mid-Holocene pedo-complex (after 3.9±0.4 ka BP.). A time gap of ca. 3.4 ka exists between this pedo-complex and the slope wash and aeolian units from the 15th century AD capping the pedo-complex. Blow outs have formed on the sparsely vegetated aeolian cover sheet and these sandy depressions are currently enlarged by wind erosion (Fig. 3). The 3.9 ka hiatus and 15th century landscape instability and their potential causes are further discussed in section 6.1

5.4 Traces of human activity at Su-re

A total of fourteen ceramic sherds were recovered from the Su-re area: samples C22 (two sherds), C23a, and C23b (six sherds) from a debris flow deposit in log R-2 and sample C28 (six sherds) from the surface of terrace 2 about 64 m northwest of log R-3 (Fig. 2, 4 and 5b; SOM 3). The sherds from C22, C23a and C23b are undecorated, have red external slips, a light brown interior slip, and have been tempered with a coarse grit. The single rim sherd from this context has a flaring, everted rim which is at a right angle to the vessel body. Finger smoothing can be observed on the flat upper surface of the rim. All samples are between 5 and 9 mm thick. The surfaces of sample C22, C23a, and C23b are partly coated with secondary calcite, because they were embedded within a sedimentary deposit for some time. The C28 sample are all body sherds are undecorated with light brown exterior slips, unslipped and unburnished interiors, and a coarse fabric with large grit inclusions. One of the sherds is a broken vessel handle.

These observations suggest that the sherds represent utilitarian ceramic and the pIRIR290 ages constrain their production (i.e. firing of the ceramic) to between 0.5 and 0.86 ka (Table 3). Similar ceramic sherds have been reported from the Yulai Cun 13-1 and the Zhongba 10-9 localities (Hudson et al., 2016), both situated in the upper Yarlung Tsangpo valley ~382 km and ~275 km northwest of Su-re, respectively. Hudson et al. (2016) assigned an age of 5.0±0.2 ka to the Yulai Cun ceramics that were recovered from a radiocarbon dated paleowetland deposit. The sherds from Zhongba are surface finds and are deemed to be ca. 1 to 1.4 ka old, based on post-IR blue OSL dating of the ceramic sherds (Hudson et al., 2016).

The cm-sized, well-rounded and mostly spheroid-shaped migmatites and leucogranites from the Greater Himalayan series that are scattered across the hillslopes of Su-re, and a high concentration in the ASF area, are erratic in nature (Fig. 3; Fig. 5e and f; Table 5). Based on lithology, they must have derived from the Cho Oyu floodplain ~1 km west of Su-re. No natural transport mechanism can be accounted for to explain (i) their position inside the Su-re catchment, that is composed of un-metamorphosed lithology only and reveals a very homogenous heavy mineral spectrum, and (ii) their stratigraphic position atop or within the aeolian cover sheet or atop the Mid-Holocene pedo-complex. Given this, it is likely that these spheroids are sling projectiles, a technology used by modern Tibetan pastoralists to herd their animals (Hummel and Vogliotti, 2000; Vega and Craig, 2009) or fragments of broken hammerstones (Table 5). The interpretation that at least some of these erratic clasts represent sling-shot projectiles is supported by analysis of the ballistic properties of sling projectiles, suggesting that ideal projectiles are spheroid-shaped with an average diameter of ~5 cm and a weight between 0.25 and 1.25 kg (Vega and Craig; 2009; Wilson et al., 2016). With few obvious exceptions (e.g. sample 013, 018 and 020; hammerstones?) most erratic clasts from Su-re match these criterions; they have an average diameter of ~5 cm and weight between 0.5 and 1.7 kg (average weight 1.0 kg, n=14; Table 5).

6 Past climate variability on the Tibetan plateau and landscape responses at Su-re

The landscape at Su-re and in the Tingri graben clearly recorded significant changes in morphodynamics over the last ca. 26 ka. These local to regional morphodynamic changes have a range of implications for high-altitude ecosystems as well as for peopling such extreme environments and need to be placed into a supra-regional paleoclimatic and paleoenvironmental context. However, the relationship of local or regional geomorphic change to supra-regional Late Quaternary climate and paleoenvironmental changes are potentially complex in nature and require further discussion, that is also summarized visually via Figure 8.

Past and present climates of the TP are strongly affected by two major atmospheric circulation systems: the Asian monsoon system and the mid-latitude westerlies. The westerlies transport moisture from the North Atlantic across Eurasia to the TP, mainly during winter and spring.

The Asian monsoon is a boreal summer phenomenon advecting heat and moist air masses into the interior of Asia between June and October from the Indian Ocean (via the Indian Monsoon branch) and the western Pacific Ocean (via the East Asian Monsoon branch), respectively (Cheng et al., 2012; Yao et al., 2013; Goswami and Chakravorty, 2018). Our understanding of the forcing mechanism of the Asian monsoon system is based on an increasing number of well-dated proxy records (particularly U-Th dated $\delta^{18}O$ records from cave calcites) and modelling studies. Collectively, these data suggest that northern hemisphere summer insolation and thus solar heating of the Asian land mass is directly affecting the mean latitudinal position and structure of the intertropical convergence zone and thus Asian monsoon variability during the Pleistocene and the Holocene (Fig. 8; e.g. Fleitmann et al., 2007; Wang et al., 2008; Cai et al., 2012; Cai et al., 2015; Cheng et al., 2016; Kathayat et al., 2016). Weak Asian monsoon intervals are accompanied by cooling events in the North Atlantic during which times the mid-latitude westerlies gain importance as moisture source for the TP, and different teleconnections between the Asian and the North Atlantic realm have been suggested (Vandenberghe et al., 2006; Cheng et al., 2009; Barker et al., 2011; Sinha et al., 2011; Kathayat et al., 2016).

While numerous continuous proxy records for Pleistocene monsoon variability from the wider Asian monsoon realm exist, very little such continuous data are available for the central high elevation portion of the TP, particularly for periods prior to the gLGM. The exceptions are a (semi-continuous) speleothem $\delta^{18}O$ record from Tianmen Cave (Cai et al., 2010; Cai et al., 2012) and a lacustrine record from Nam Co Lake (Zhu et al., 2015), both situated on the south central TP ~450 km northeast of Su-re. The Tianmen record covers the Marine Isotope Stages (MIS) 5e, 5c and 5a, indicating that during the last interglacial and subsequent interstadials the ISM intensity and temperature were high enough to facilitate precipitation of cave calcite at ~4800 m asl (Cai et al., 2010). The study of Zhu et al. (2015) spans the past 24 ka and suggests a strong influence of the westerlies under a cold and dry climate between 24 and 16.5 ka and an increasing influence of the ISM thereafter, which brought about increasingly warmer and wetter climatic conditions to the central TP.

The Tianmen and Nam Co records demonstrate the importance of the Asian monsoon and the mid-latitude westerlies as well as of northern hemisphere temperature changes for Tibet. Such orbital to millennial scale changes in temperature and hydroclimatic conditions are also impacting on Himalayan and Tibetan glaciers and reflected in the Quaternary glacial history of the Cho Oyu-Everest massif. Owen et al (2009) constrained the depositional age of four glacial stages in the Rongbuk valley on the northern flank of Mount Everest ~34 km southeast of Su-re (Fig. 1 and 8; Jilong: 24-27 ka, Rongbuk: 14-17 ka, Samdupo, subdivided into Samdupo I: 6.8-7.7 ka and Samdupo II: ca. 2.4 ka and Xarlungnama: ca. 1.6 ka) and correlated these stages with moraines from the southern slopes of Everest. They also observed an absence of early Holocene glacier advances north of Mount Everest. The data from Owen et al (2009) thus suggest that glaciers in the Rongbuk valley are topographically sheltered (largely cut off from the influence of a strong ISM during e.g. the early Holocene), and hence reveal a greater sensitivity to northern hemisphere cooling signals, compared to the monsoon dominated glaciers at the southern flank of the Everest massif.

For the Holocene numerous and (semi-)continuous monsoon proxy records from the TP and the adjacent Himalaya are available, against which the Su-re sediment record can be compared. Most of these records are based on lacustrine archives (e.g. Morrill et al., 2003; Shen et al., 2008;

Mügler et al., 2010; Wünnemann et al., 2010; Rades et al., 2013; Bird et al., 2014; Hudson et al., 2015; Huth et al., 2015; Li et al., 2016; Shi et al., 2017; Conroy et al., 2017) and in a few cases on speleothem $\delta^{18}O$ records (Cai et al., 2012; Kathayat et al., 2017). These data indicate (i) a precipitation maximum in the early Holocene, as boreal summer insolation peaked, followed by (ii) a decline in precipitation through the mid- to late-Holocene in tandem with the decreasing northern hemisphere summer insolation and a southward migration of the intertropical convergence zone, and (iii) millennial to centennial scale patterns in most of these proxies, often expressed as punctuated droughts or prolonged monsoon weakening events. Among these events is a prominent weakening in monsoon strength between ca. 3.9 and 4.2 ka, which is recorded in several of the afore mentioned archives from the TP (Morrill et al., 2003; Shen et al., 2008; Mügler et al., 2010; Wünnemann et al., 2010; Cai et al., 2012; Bird et al., 2014; Shi et al., 2017) and also documented in many other ISM records beyond the TP (e.g. Staubwasser et al., 2003; Fleitmann et al., 2007; Dixit et al., 2014; Donges et al., 2014).

As far as the modern climatic regime of the TP is concerned, stable isotope measurements in precipitation suggest two distinct climatic regions, with a boundary approximately along the southern Tanggula Mountains (Fig. 1). In the southern region, the influence of the ISM gradually increases southward, while in the northern region, the climate is dominated by westerlies and continental air masses (Tian et al., 2001; Yu et al., 2008; Yao et al., 2013). These isotopic data (Tian et al., 2001; Yao et al., 2013) as well as satellite observations (Tropical Rainfall Measurement Mission; Bookhagen and Burbank, 2010; Hudson and Quade, 2013) and high-resolution atmospheric datasets (High Asia Reanalysis; Maussion et al., 2014), suggest that modern precipitation in southern Tibet, including Su-re, is mostly transported along the Brahmaputra River valley and advected across Himalayan passes via the ISM.

Given the geographic position of Su-re at the southern rim of the TP and immediately north of Nangpa La and the modern monsoon trajectories, it is plausible to suggest that the ISM plays an important role in controlling moisture availability and thus affecting earth surface processes in southern Tibet not only today, but also during the Holocene and the Pleistocene. A high sensitivity of earth surface processes and the cryosphere to changes in ISM intensity during the Late Pleistocene and Holocene has already been demonstrated by e.g. Owen et al. (2009) and Wang et al. (2017) for southern Tibet. From our data collected in Su-re and the Tingri graben we infer three types of monsoon related millennial to centennial scale landscape responses involving specific interactions between monsoonal climate and geomorphological agents: (i) monsoon-vegetation-soil interactions, and monsoon governed interactions between (ii) soil moisture and permafrost and (iii) between hydro-climate and sediment transport. These climatic-geomorphological interrelations are discussed in the following and placed into a regional paleoclimatic and paleoenvironmental context.

6.1 Climate-vegetation-soil interactions

A pedo-complex at Su-re evolved from ca. 6.4 ka until 3.9 ka BP and reflects slow sediment accretion on hillslopes with contemporaneous (cumulic) soil formation leading to a marked Bv horizon containing evidence for the presence of *Picea* ca. 6 ka ago (Fig. 8). Data on aeolian activity and pedogenesis in southern Tibet are relatively scant compared to the north and northeastern sectors of the plateau (Stauch, 2015). However, the available studies suggest enhanced aeolian sand accumulation in southern Tibet from 31.6 to 12.7 ka and from 9.2 to 6.2 ka, with an eventual peak in aeolian activity at 7.5 ka (Stauch, 2015). This fits our observation based on the Su-re sedimentary record, suggesting that until ca. 6.4 ka the landscape of Su-re was largely vegetation free and characterized by permafrost and periglacial activity. Currently, only one study provides age constraints on pedogenesis in southern Tibet; i.e. Pan et al. (2013) investigated aeolian sand deposits in the Dinggye area ca. 120 km east of Su-re and report a main period of pedogenesis from 6.6 to 4.9 ka BP in agreement with our observations. Data from Su-re and the adjacent Dinggye area thus hint towards favorable (warm and wet) paleoenvironmental conditions allowing for an increased vegetation cover with tree stands of *Picea* for the duration of several millennia during the mid-Holocene. We argue that an increase in monsoon related effective precipitation is causing the vegetation cover to expand thus stabilizing the landscape, allowing aeolian (and/or slopewash) sediments to become trapped, and resulting in the formation of a cumulic soil. A reversal of these processes in the case of a long-lasting negative effective precipitation regime contributes to landscape and soil degradation and thus a negative bio-pedogenetic feedback loop (i.e. erosion).

The Mid-Holocene pedo-complex at Su-re is truncated by a hiatus at 3.9±0.4 ka BP (Fig. 8). This date coincides with the prominent weakening in monsoon strength between ca. 3.9 ka and 4.2 ka discussed above (Morrill et al., 2003; Shen et al., 2008; Mügler et al., 2010; Wünnemann et al., 2010; Cai et al., 2012; Bird et al., 2014; Shi et al., 2017) and initiated a negative bio-pedogenetic feedback loop. This reasoning is in-line with observations of Pan et al. (2013), who report enhanced aeolian activity in the Dinggye area since 2 ka BP and the development of moving dunes due to an increasingly cool and dry climate. Furthermore, we note that the glacial advances Samdupo I (7.7 – 6.8 ka) and Samdupo II (2.4 ka) in the Rongbuk valley (Owen et al., 2009) occurred immediately before and after the phase of mid-Holocene soil formation at Su-re (3.9 to 6.4 ka BP). The Samdupo glacial stages with their supposed link to northern hemisphere cooling (Owen et al., 2009) are thus bracketing the Su-re pedo-complex (Fig. 8), for which we suggest comparatively milder and wetter climatic conditions.

6.2 Soil moisture-permafrost interactions

Our optical ages from the organic-free and cryoturbated sediments of Su-re fall into two groups: one covers the time range from 18–26 ka, and thus coincides with the gLGM; the second group clusters at 11 ka, and thus coincides precisely with the beginning of the Holocene (Fig. 8). No sedimentary evidence for intensive cryoturbation during the rest of the Holocene has been found. We propose that a causal mechanism between monsoon intensity, soil moisture and permafrost and/or periglacial activity can account for this pattern. The arid character of the TP results in an ice-poor and thin permafrost layer, where mid-portion contraction of the active layer does not occur to the same extent as in high latitudes, which in turn is suppressing permafrost features and periglacial processes on the plateau (Wang and French, 1995b; Wang and French, 1995c). Variation in soil moisture availability in such arid settings should thus impact on the ice-content of the active layer and periglacial and permafrost related process rates. In this model that has been indirectly suggested by Wang and French (1995b) already, wetter conditions on the TP will cause cryoturbation, frost heave and solifluction processes to intensify and valley slope denudation to accelerate. At Su-re, the ISM maximum of the early Holocene would have caused a sudden increase of soil moisture and thus ice-content of the active layer in the hill slopes of Su-re, triggering an increase in periglacial and permafrost processes. Further warming and a gradual decrease in moisture availability over the course of the Holocene counteracted this initial intensification of permafrost processes. We argue that this speed-up/intensification of periglacial processes during the early Holocene was a transient phenomenon. On the other hand, our data also demonstrate that under cold and dry climatic regime of the gLGM on the TP (Cai et al., 2010; Cai et al. 2012; Zhu et al., 2015), cryoturbation and solifluction was ubiquitous at Su-re, regardless of the (probably strongly reduced) soil moisture availability during this time.

For Su-re we calculated a depression of ~240 – 330 m for the discontinuous permafrost zone during the gLGM relative to today (section 5.1). Thus, the lower limit of discontinuous permafrost would have shifted from ~4980 – 4800 (today) to ~4470 – 4740 m asl. (gLGM) and eventually Su-re itself (4450 m asl.), but certainly the surrounding hill slopes would have been entirely integrated into the discontinuous permafrost belt during the gLGM. In combination with (even slightly) enhanced moisture transport onto the TP by the westerlies during the gLGM compared to today (e.g. Vandenberghe et al., 2006, Zhu et al., 2015) the ubiquitous occurrence of sedimentary periglacial and permafrost features of Su-re dating into the gLGM can be explained.

6.3 Hydro-climate - sediment transport interactions

Via OSL dating we constrained the age of most of the organic-free hillslope sediments at Su-re and the fluvial terraces next to the ASF area to the last gLGM (section 5.1). CRN dating of the Cho Oyu lateral moraine (Chevalier et al, 2011) and the Jilong glacial stage at the north face of Everest (~34 km southeast of Su-re; Owen et al., 2009) suggest a major glacial advance in the Cho Oyu-Everest massif between 24 and 27 ka (Fig. 8). The gLGM in the wider Su-re area was thus characterized by enhanced hillslopes dynamics, a lack of vegetation and widespread glacial advance. In combination with a generally weak ISM during the gLGM (e.g. Wang et al., 2008; Kathayat et al., 2016), hence low fluvial discharge rates, instantaneous and strong valley floor aggradation in the Tingri graben and its tributaries was the result (Fig. 8). A strong correlation between climate and river activity on orbital to sub-orbital timescales, with fluvial aggradation and incision being linked to cold and warm climatic periods, respectively, has long been established (e.g. Maizels, 1979), but more complex control mechanism for terrace formation have been invoked too (e.g. Pratt-Sitaula et al., 2004; Rixhon et al., 2011). On these timescales the relevant controlling factors on fluvial dynamics include river run-off (stream power), sediment supply, vegetation cover and permafrost conditions, and each of these factors is in turn influenced by the catchment-scale climate (e.g. Vandenberghe 2002; Vandenberghe 2003; Pratt-Sitaula et al., 2004).

Subsequent to the gLGM river incision lowered the Su-re valley floor by ~10-20 m and left the fill-terrace (T3) and cut-terraces (T1 and T2; Fig. 2). We speculate that only the strengthening of the ISM during the early Holocene provided enough stream power to start and accomplish this incision process. Such a mechanism of major river incision and terrace formation steered by the ISM during phases of maximum monsoon strength has been demonstrated by Wang et al. (2017) for the upper Sutlej valley (Tirthapuri, ~640 km east of Su-re) in the arid southwestern TP, already. Wang et al (2017) investigated a flight of fluvial terraces capped by travertine deposits and used U-Th and OSL dating to constrain major pulses of fluvial incision at Tirthapuri, to ca. 127.5 ka and between ca. 8.8

and 10.0, coincident with the last interglacial (MIS 5e) and the early Holocene ISM maxima. Furthermore, in Tirthapuri as in Su-re hillslope processes were enhanced during this time period as demonstrated by OSL dated alluvial fan deposits in Tirthapuri (9.1±0.7 ka; Wang et al., 2017) and intensification of periglacial hillslope processes at Su-re (at 11-10 ka; sections 5.2). Because the climatic setting and landscape dynamics of Tirthapuri and Su-re are fairly similar, we tentatively invoke the same monsoon-related incision process during the early Holocene at Su-re too.

7. A case for anthropogenically induced landscape degradation in the 15th century AD?

The sedimentary and geomorphological record of Su-re suggests that the time period subsequent to 3.9±0.4 ka was characterized by erosion. The hiatus truncating the Mid-Holocene pedo-complex is attributed to the. 3.9–4.2 ka monsoon weakening event (section 6.1). The aeolian cover sheet that blankets this pedo-complex and covers large parts of the landscape in the Tingri graben, as well as the alluvial fan deposit at Su-re, both ca. 0.5 ka in age, indicate another phase of landscape instability (section 5.3). We have no information about the landscape dynamics at Su-re between 0.5 and 3.9 ka.

It is tempting to correlate this youngest erosional phase at Su-re with the Little Ice Age (LIA; i.e. the past ca. 0.7 ka until 1950 AD.; Matthews and Briffa, 2005; Xu and Yi, 2014). In a high-resolution speleothem $\delta^{18}O$ record from Sahiya cave, located at 1190 m asl in the southern foothills of the western Himalaya, ~860 km west of Su-re (Fig. 1a), the LIA cold period is particularly well resolved (Kathayat et al., 2017). Because of its position at the fringe of the ISM realm, the Sahiya record is deemed a sensitive indicator of ISM variability (Kathayat et al., 2017) and can thus be regarded as a good monsoon intensity proxy in the arid setting of Su-re too (Fig. 8). The Sahiya record covers the past 5.7 ka and chronicles the LIA as a prolonged phase of ISM weakening starting at ca. 0.8 ka attaining an absolute minimum at 0.35±0.02 ka BP (~1593 to 1623 AD; Kathayat et al., 2017). In the wider Asian monsoon realm the onset of the LIA ca. 0.7 ka ago is accompanied by a series of long-term droughts (i.e. from the mid-14th to 15th centuries onward), of which the Sahiya megadrought at 0.35 ka BP is one of them the latter also coincides with the collapse of the Guge empire in western Tibet (Fig. 8; Kathayat et al., 2017; Sinha et al., 2011; Yadava et al., 2016). Nevertheless, droughts were not restricted to the LIA cooling period alone but occurred repeatedly during the late Holocene in the Asian monsoon regions (Sinha et al., 2011; Kathayat et al., 2017). Taking the central weighted mean age of the aeolian cover sheet and debris flow deposit and associated standard deviation (0.56±0.08 ka; 1376 to 1536 AD) the Sahiya megadrought but also droughts from the 14th and 15th century AD could be invoked for causing landscape degradation at Su-re.

While purely climatically induced landscape degradation is a plausible explanation for the 3.9±0.4 ka and 0.56±0.08 ka (ca. 1376 to 1536 AD) erosional events, we believe that a series of observations from Su-re call for a more nuanced interpretation, particularly with regard to the 0.56±0.08 ka (ca. 1376 to 1536 AD) erosional events. The pottery sherds from Su-re are between 0.50 and 0.86 ka in age (end of the 12th beginning of the 16th and century), and several are incorporated in the 0.61±0.08 ka (ca. 1328 to 1488 AD) old debris flow deposit. The close match of the pottery and debris flow ages implies human presence during or immediately before the debris flow event. Also, the possible sling shot projectiles and other artifacts are all concentrated in the ca.

0.56±0.08 ka (ca. 1376 to 1536 AD) old aeolian cover sheet or occur in chronostratigraphic positions < 3.9 ka. These lines of evidence suggest human presence at Su-re subsequent to 3.9 ka BP and a potentially intensive anthropogenic use of the landscape prior to 0.56±0.08 ka (ca. 1378 to 1538 AD). Palynomorphs indicate the presence of *Picea* ca. 6 ka ago, whereas the modern vegetation lacks any shrubs or trees and is composed of a sparse and highly discontinuous grass cover only. The thickness (up to 1.8 m at Su-re) and spatial extent of the aeolian coversheet deposit further indicate that the destabilization phase is a high magnitude and regional event.

In combination, we hypothesize that (i) the Su-re and Cho-Oyu outwash plains and the climatic extremes that ramped up in the course of the LIA provide the underlying susceptibility to sand drifting in the Tingri graben, which was (ii) paired with a strong anthropogenic imprint that ultimately led to a strong erosional event. Similar environmental feedback mechanism involving aeolian activity and landscape degradation have been described for e.g. Medieval Europe (DeKeyzer and Bateman, 2018; Lungershausen et al., 2018; Pierik et al., 2018). In sensitive high-mountain ecotones such as the Himalaya or the TP, the overuse of wetlands and adjacent hillslopes by yak pastoralists (i.e. a setting such as Su-re) can trigger a non-linear regime shift in landscape dynamics, initiating widespread erosion (e.g. Löffler, 2000; Byers, 2005; Zhou et al., 2005). Furthermore, as a site associated to a wetland, Su-re also lies on the trade route linking Tibet with Nepal via Nangpa La, and might thus have already experienced above-average grazing pressure by nomads and merchants and their caravans on their way from north to south and vice versa, making sites like Su-re particularly susceptible to climatically induced soil degradation. The ongoing deflation, documented by the high density of active blow-outs, the absence of modern soil formation and a lack of any significant stabilizing vegetation suggests that the landscape at Su-re has not yet recovered from the degradation event that was initiated during the 15th century AD.

Our hypothesis of a non-linear but unidirectional regime shift due to the combined effect of LIA cooling and an anthropogenic overuse of the landscape is supported by maps and documents that chronicle the spatio-temporal economic and societal changes in Tibet since the 6th century AD (Ryavec, 2015, p.16). For south-central Tibet these data show a strong increase in the number of Buddhistic temples and monasteries from the 10th until the mid-14th century AD and a sharp decline in the century thereafter. Monasteries were always the social, political and economic hubs in historic Tibetan societies; hence their number reflects economic and demographic long-term trends (Ryavec, 2015). The 15th century environmental degradation seen in southern Tibet at Su-re and a concomitant decline in temple and monastery construction might well be causally linked (Fig. 8).

Finally we note that genetic data and ethnographic accounts suggest that the Sherpas, which is an ethnic group living in the Khumbu Himalaya today (i.e. the Nepalese part of the Cho-Oyu Mount Everest massif), left their ancestral Tibetan homeland via a series of migration events. These migrations have been constrained to <1.5 ka and ca. 0.94 ka ago by genetics (Bhandari et al., 2015), while recent historical records describe major Sherpa migrations from eastern Tibet (Kham) into the Tingri region, from where the Sherpas entered the Khumbu Himalaya via the Nangpa La pass during 16th century (Oppitz, 1974; Gautama and Thapa-Magar, 1994). Again, these dates broadly coincide with the onset of the LIA ca. 0.8 ka ago and overlap with the onset of environmental degradation dated by us to ca. 0.56±0.08 ka ago (ca. 1378 to 1538 AD; Fig. 8).

8. Conclusions

The Tingri graben and the archaeological site of Su-re are situated in the rain shadow of the Greater Himalaya and thus receive a limited amount of precipitation from the ISM. This arid high-altitude ecosystem is characterized by cold climate earth surface processes. On orbital to millennial time scales temperature fluctuations exerted a strong control on the morphodynamics of this area; e.g. the temperature decline of the gLGM governed a complex reaction of the sediment cascade, involving glacial advance and formation of massive hummocky moraines, intensification of periglacial and permafrost hill slope processes and valley floor aggradation. For the LGM we tentatively quantified the depression of the permafrost zone for the Su-re area to ~344±109 m relative to today. In contrast, expansion of a vegetation cover with cumulic soil formation (from ca. 6.7–3.9 ka) characterizes the most favorable climatic phases, such as the Mid-Holocene. High sensitivity of the southern Tibetan realm to northern hemisphere cooling also during the Holocene is further inferred from comparison of the sedimentary data from Su-re with aeolian and glacial records from the adjacent Dinggye area (Pan et al., 2013) and the north flank of Mount Everest (Rongbuk valley; Owen et al., 2009). Collectively, these data suggest that formation of the Mid-Holocene pedo-complex at Su-re (ca. 3.9 to 6.4 ka) was bracketed by enhanced aeolian activity in Dinggye and temperature controlled glacial advances in the Rongbuk valley (northern slopes of Mount Everest).

Because of the aridity in southern Tibet, little effective precipitation and thus soil moisture is available for segregated and pore ice formation and vegetation growth. For the same reason surface runoff and discharge are greatly reduced in this sector of the TP. Hence, high-altitude landscape dynamics and earth surface processes in the wider Su-re area are moisture limited, yet sensitive to temperature changes. We identify three types of landscape-climate interactions in our investigation area that are strongly linked to effective precipitation and thus to (millennial scale) fluctuations in ISM intensity: (i) monsoon-vegetation-soil interactions, and monsoon governed interactions between (ii) soil moisture and permafrost as well as periglacial activity and (iii) between hydro-climate and sediment transport. Our data suggest that these interactions are short term transient geomorphological changes driving unidirectional non-linear climate-landscape responses.

Furthermore, we speculate that during the Late Holocene, but definitely during the LIA the anthropogenic pressure on the sensitive high-altitude ecosystem of the wider Su-re area was steadily increasing, eventually dipping the ecological system and earth surface processes out of balance leading to widespread landscape degradation and soil deflation. The dominance of erosional processes since the 15th century AD., and the absence of notable vegetation in the modern landscape of the Tingri-Su-re area are tentatively interpreted as the result of a climatically prepared but anthropogenically triggered ecological collapse in southern Tibet. Interestingly, during the 15th century migration of the Sherpas into the Tingri graben and subsequently into the Khumbu Himalaya as well as a sudden decline in temple and monastery construction in southern Tibet occur too (Oppitz, 1974; Bhandari et al., 2015; Ryavec, 2015).

Deciphering the (often non-linear) impact of the various climatic drivers on geomorphic processes and disentangling (complex) human-environment interrelations in the sensitive high-altitude ecosystems of the TP are non-trivial tasks. Achieving these tasks will require much more empirical and analytical data on landscape-scale processes and should be based on a careful examination of a range of sedimentary archives (including soils, paleosols and periglacial sediments) and geomorphological and archaeological features and even ethnographic accounts and a combination of multiple proxy records with reliable chronological control. So far, most paleoenvironmental TP studies have focused on long and continuous single archives (such as lake, pollen or speleothem records) or used a single-proxy approach (most studies on aeolian or glacial activity). Targeting multiple archives and investigating the interactions between different earth surface processes and the role of humans on the TP are research tasks hitherto tackled much less frequently by the earth science community working on the TP. Most striking is (i) the circumstance that permafrost and periglacial processes are ubiquitous and of major importance for the landscape dynamics on the TP (Wang and French, 1995b), yet are severely under-researched on Quaternary timescales and (ii) little and only contradictive information is available regarding the time-depth and magnitude of a potential human impact on Tibet´s sensitive high-altitude ecotone (e.g. Herzschuh et al., 2011; Miehe et al., 2014). Therefore, our approach is exemplary and furthers our understanding of the details and nature of Late Quaternary changes in landscapes and ecosystems involving humans in the largest high-altitude landmass on our planet.

Acknowledgements

This research was funded by Austrian Science Fund grants to M.C.M. (FWF grant 24924-G19) and L.A.G. (FWF grant M2121-G25) as well as the Tirolian Science Fund grant to M.C.M. (TWF UNI-0404/1355). Parts of this research were carried out at the Ion Beam Centre (IBC) at the Helmholtz-Zentrum Dresden–Rossendorf e.V., a member of the Helmholtz Association. We thank K. Pellegrini and S. Gehring for lab support and are grateful to A. Gärtner, R. Llovera, A. Scharf, C. Tiessen, R. Ziegenrücker, and the DREAMS operator team (HZDR) for their help during AMS measurements and S. Gurlit (HZDR) for performing ICP-MS measurements. We thank Jan Blöthe and an anonymous reviewer for their helpful comments that improved this paper.

Figure captions

Figure 1A: The Tibet-Himalaya orogen with sites mentioned in the text (numbered 1 to 6): 1 = Tingri basin and the archaeological site of Su-re (this study); 2 = aolian record from the Dinggye area (Pan et al., 2013); 3 = ceramic sherds from the Yulai Cun 13-1 site (Hudson et al., 2016); 4 = ceramic sherds from the Zhongba 10-9 site (Hudson et al., 2016); 5 = Tianmen speleothem records (Cai et al., 2010; Cai et al., 2012); 6 = lacustrine record from Nam Co Lake (Zhu et al., 2015); 7 = Sahiya speleothem record (Kathayat et al., 2017); 8 = travertine deposits and fluvial terraces at Tirthapuri, upper Sutlej valley (Wang et al., 2017). B: Oblique aerial view over the Tingri graben and Mount Everest-Cho Oyu massif (Google Earth). View is to the south. Dotted lines outline the Cho Oyu and Lapchi hummocky moraine lobes as well as the Jilong glacial stage.

Figure 2: Geomorphological overview map of the wider Su-re area. The positions of the sedimentary logs discussed in the text are indicated (Base map: Google Earth).

Figure 3: Geomorphological detail map of Su-re and area with archaeological surface finds (ASF). The positions of the sedimentary logs discussed in the text are indicated (Base map: Google Earth).

Figure 4: Sedimentary logs of Su-re. For location of logs on geomorphological maps and field context see figure 2 and 3.

Figure 5A: Geomorphological map of the Cho Oyu hummocky moraine and CRN sampling positions. B: Elevation profile across the Cho Oyu hummocky moraine (profile line indicated in figure 5A).

Figure 6: Selected field images from the Su-re area. 6A: Gravelly fluvial terrace sediment (log R1) with cryoturbated sand layer. Camera bag for scale. 6B: Gravelly fluvial terrace sediment (log R2) overlain by debris flow deposit (white arrow) containing red ceramic (white circle). Cap for scale. 6C: Sediment outcrop in gully 2 (log G-2B) composed of (bottom to top): sterile cryoturbated sediments, organic rich blackish horizon, reddish Bv-horizon, yellowish debris flow deposits. Spate for scale. 6D: Aeolian cover sheet, 1.8 m in thickness (log Bo-180). See also figure 4 for sediment logs and figures 2 and 3 for positions of sediment outcrops in landscape. 6E: View over the area with high density of archaeological surface finds. Note quartzite boulders in background that were in use as a lithic quarry site. View is towards northwest. 6F: Leucogranitic spheroid, interpreted as sling shot projectile. 6G: Quartzite boulder that revealed negative flake scars after sampling for OSL rock surface dating (Gliganic et al., 2019).

Figure 7: OSL data. Representative decay curves (A), dose-response curve (B), and De distribution shown as a radial plot (C) for a representative sample (TIN8). The grey bar in (C) is centered on the CAM. (D) shows the De distribution for sample TIN4y, which has two apparent populations of De values – see text for discussion. The grey bars in (D) are centered on the CAM of each population.

Figure 8: Overview of selected monsoon records and comparison with paleoenvironmental processes and events in the Su-re/Tingri area. a) Composite Chinese speleothem record (Wang et al., 2008); b) Speleothem record from the Tianmen, central Tibet (Cai et al., 2012); c) Speleothem record from Sahiya cave, northwestern Subhimalaya (Kathayat et al., 2017). Note that high $\delta^{18}O$ values correlate with low monsoon intensities (and vice versa) and can be correlated with cooling events in

the northern hemisphere. Selected northern hemisphere cooling events are indicated on the Sahiya speleothem record (grey vertical bars): LIA = little ice age; DACP = Dark Age Cool Period; CP = further cool periods.

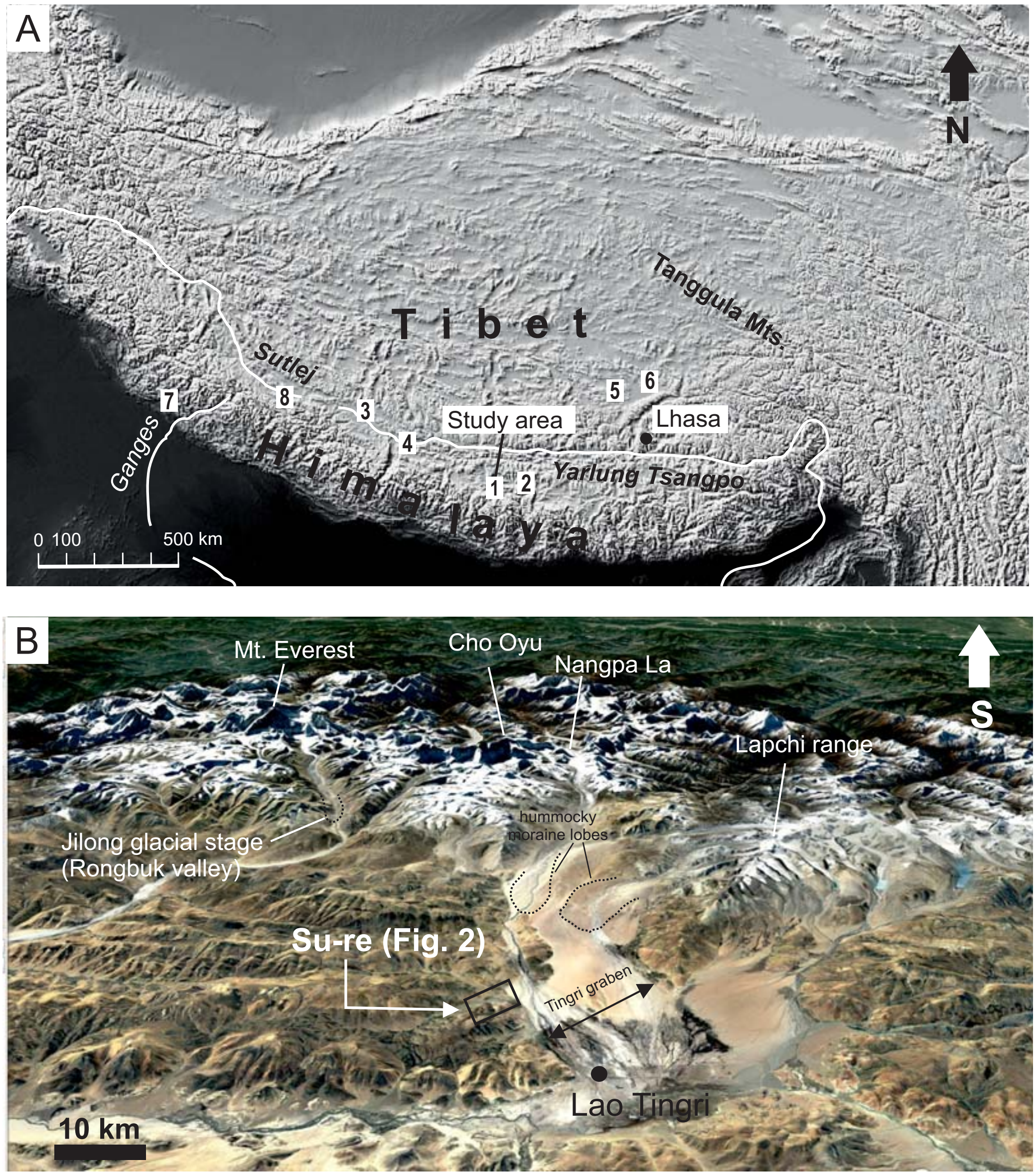
A
N
Tibet
Tanggula Mts.
Sutlej
Ganges
Himalaya
Yarlung Tsangpo
Study area
Lhasa
1
2
3
4
5
6
7
8
0 100 500 km
B
Mt. Everest
Cho Oyu
Nangpa La
S
Lapchi range
hummocky moraine lobes
Jilong glacial stage (Rongbuk valley)
Su-re (Fig. 2)
Tingri graben
Lao Tingri
10 km

Figure 1

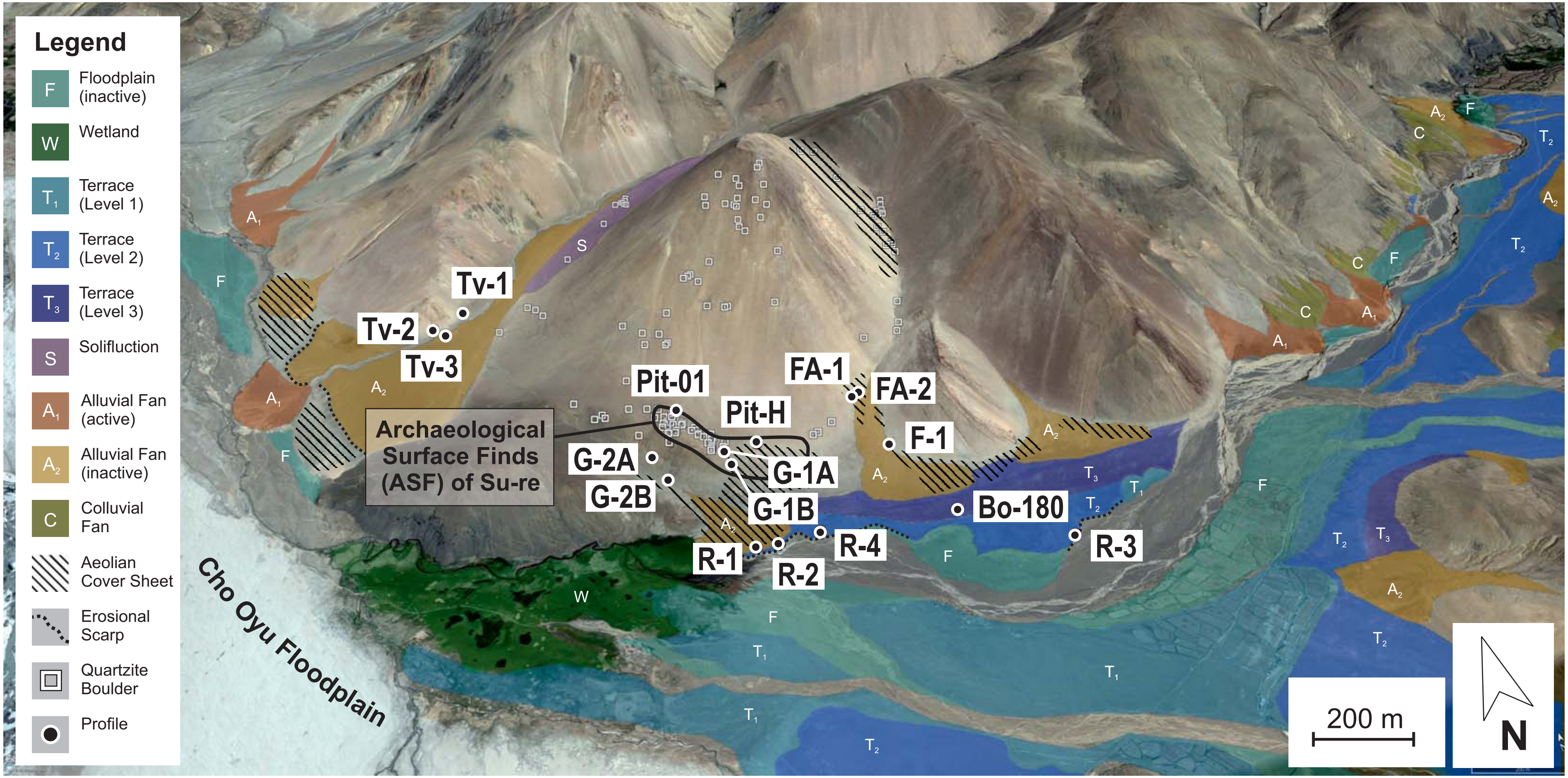

Legend
F
Floodplain (inactive)
W
Wetland
T1
Terrace (Level 1)
T2
Terrace (Level 2)
T3
Terrace (Level 3)
S
Solifluction
A1
Alluvial Fan (active)
A2
Alluvial Fan (inactive)
C
Colluvial Fan
Aeolian Cover Sheet
Erosional Scarp
Quartzite Boulder
Profile
Tv-1
Tv-2
Tv-3
Pit-01
FA-1
FA-2
Pit-H
F-1
Archaeological Surface Finds (ASF) of Su-re
G-2A
G-2B
G-1A
G-1B
Bo-180
R-1
R-2
R-3
R-4
Cho Oyu Floodplain
200 m
N

Figure 2

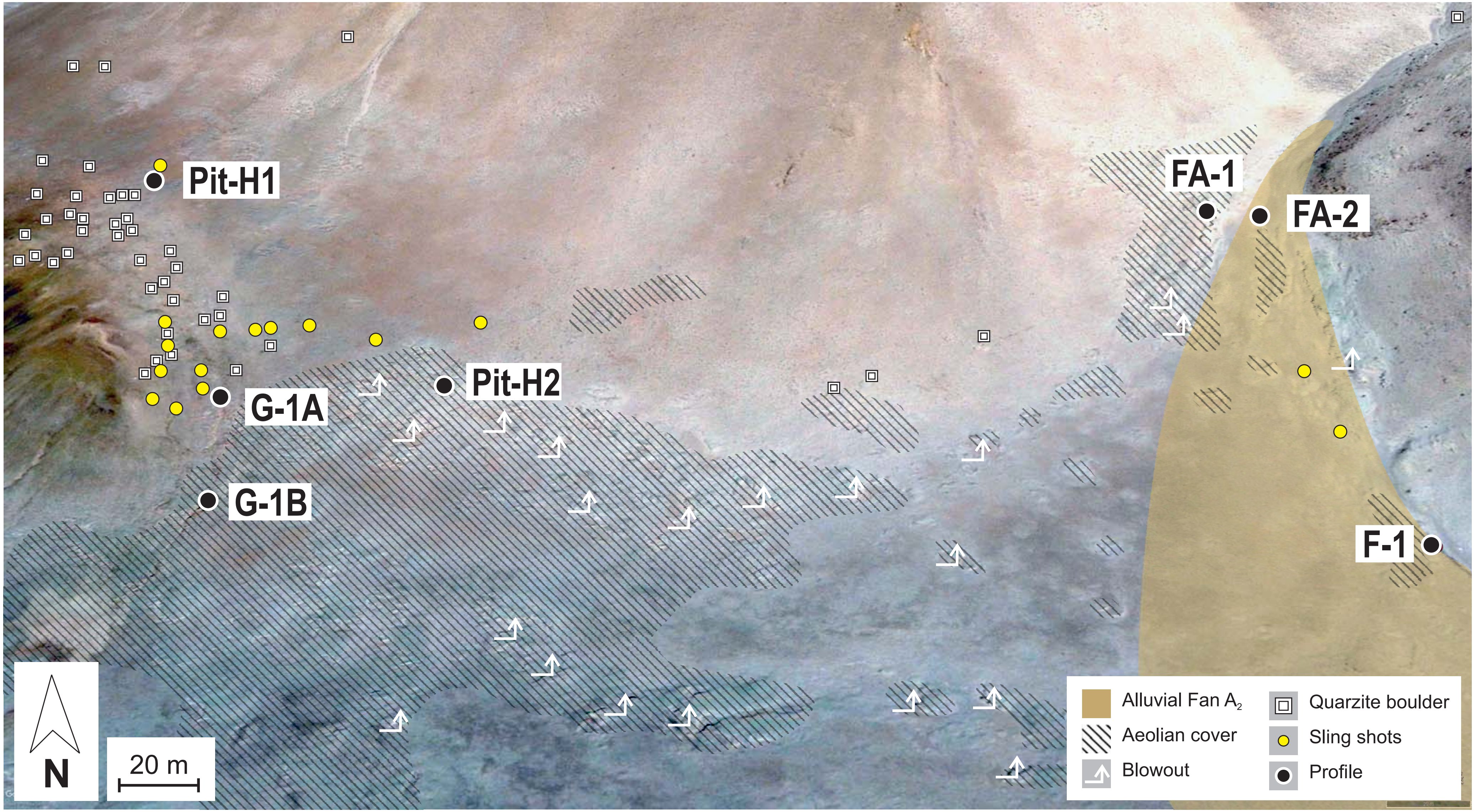

Pit-H1
Pit-H2
G-1A
G-1B
FA-1
FA-2
F-1
N
20 m
Alluvial Fan A_2
Aeolian cover
Blowout
Quarzite boulder
Sling shots
Profile

Figure 3

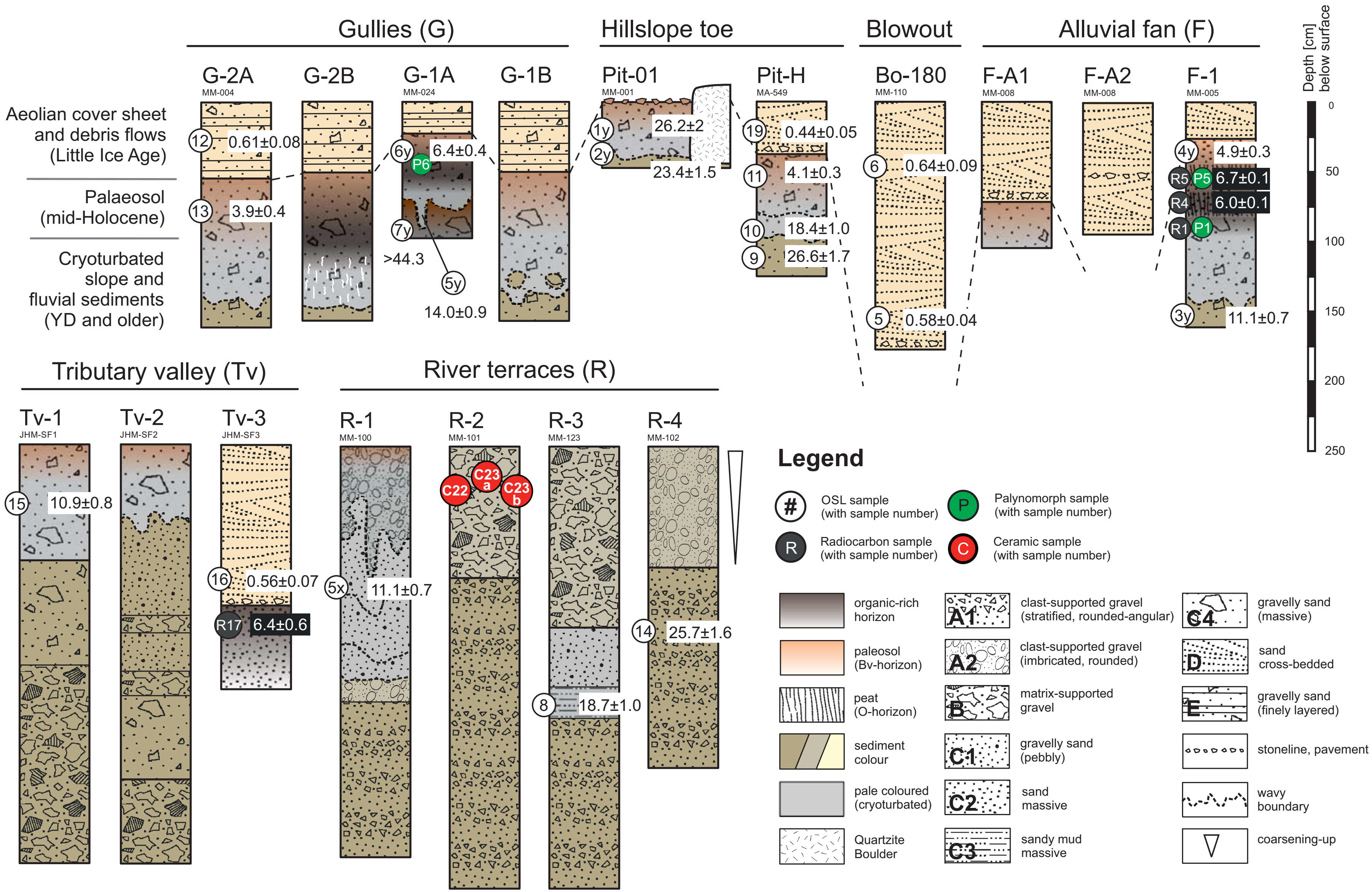

Gullies (G)
Hillslope toe
Blowout
Alluvial fan (F)
G-2A
MM-004
G-2B
G-1A
MM-024
G-1B
Pit-01
MM-001
Pit-H
MA-549
Bo-180
MM-110
F-A1
MM-008
F-A2
MM-008
F-1
MM-005
Aeolian cover sheet and debris flows (Little Ice Age)
Palaeosol (mid-Holocene)
Cryoturbated slope and fluvial sediments (YD and older)
0.61±0.08
3.9±0.4
6.4±0.4
>44.3
14.0±0.9
26.2±2
23.4±1.5
0.44±0.05
4.1±0.3
18.4±1.0
26.6±1.7
0.64±0.09
0.58±0.04
4.9±0.3
6.7±0.1
6.0±0.1
11.1±0.7
Depth [cm] below surface
Tributary valley (Tv)
River terraces (R)
Tv-1
JHM-SF1
Tv-2
JHM-SF2
Tv-3
JHM-SF3
R-1
MM-100
R-2
MM-101
R-3
MM-123
R-4
MM-102
10.9±0.8
0.56±0.07
6.4±0.6
11.1±0.7
18.7±1.0
25.7±1.6
Legend
OSL sample (with sample number)
Palynomorph sample (with sample number)
Radiocarbon sample (with sample number)
Ceramic sample (with sample number)
organic-rich horizon
paleosol (Bv-horizon)
peat (O-horizon)
sediment colour
pale coloured (cryoturbated)
Quartzite Boulder
clast-supported gravel (stratified, rounded-angular)
clast-supported gravel (imbricated, rounded)
matrix-supported gravel
gravelly sand (pebbly)
sand massive
sandy mud massive
gravelly sand (massive)
sand cross-bedded
gravelly sand (finely layered)
stoneline, pavement
wavy boundary
coarsening-up

Figure 4

Figure 5

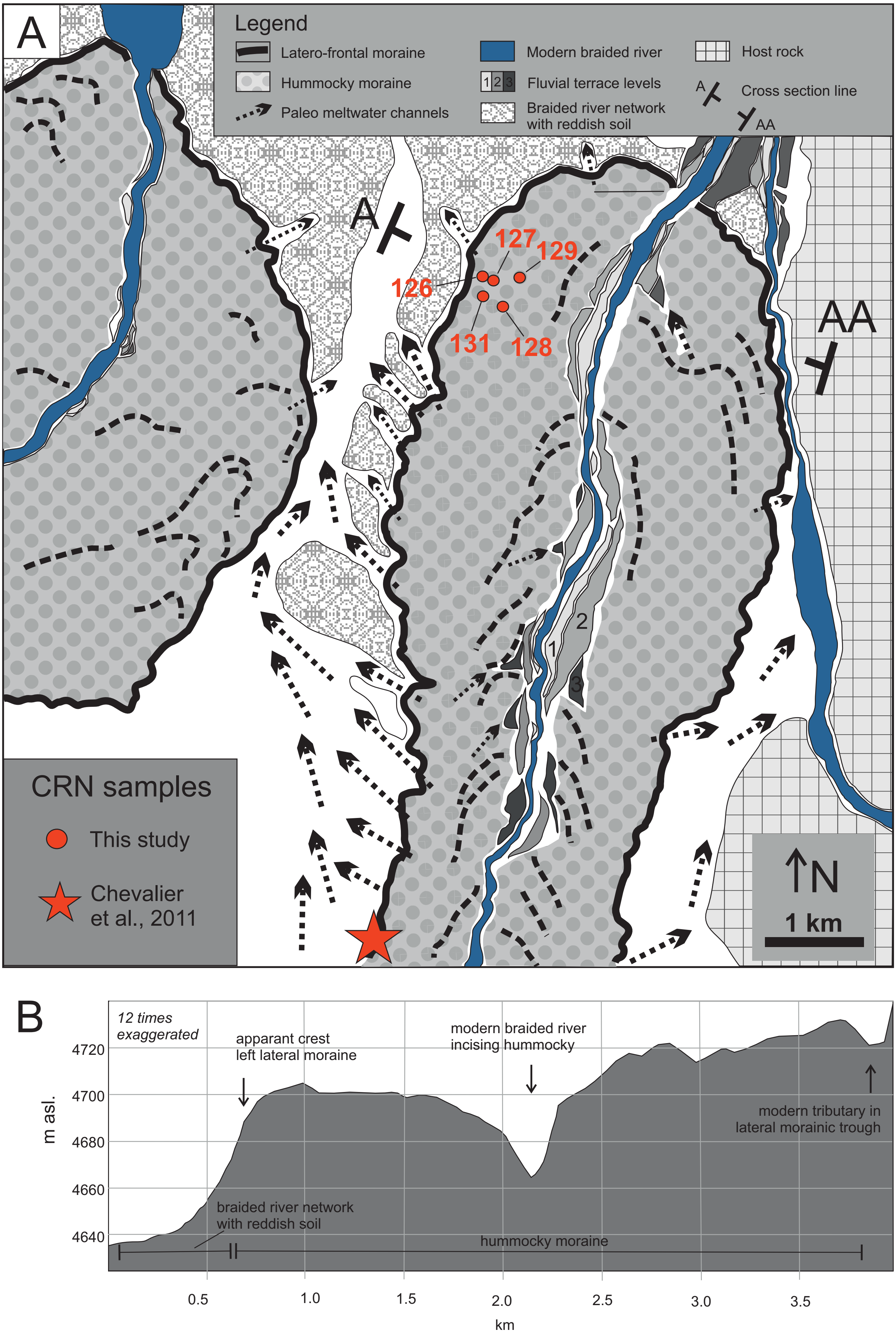
A
Legend
Latero-frontal moraine
Hummocky moraine
Paleo meltwater channels
Modern braided river
1 2 3
Fluvial terrace levels
Braided river network
with reddish soil
Host rock
A
Cross section line
AA
A
127
129
126
131
128
AA
2
1
3
CRN samples
This study
Chevalier
et al., 2011
N
1 km
B
12 times
exaggerated
apparent crest
left lateral moraine
modern braided river
incising hummocky
modern tributary in
lateral morainic trough
braided river network
with reddish soil
hummocky moraine
m asl.
4720
4700
4680
4660
4640
0.5
1.0
1.5
2.0
2.5
3.0
3.5
km

Figure 6

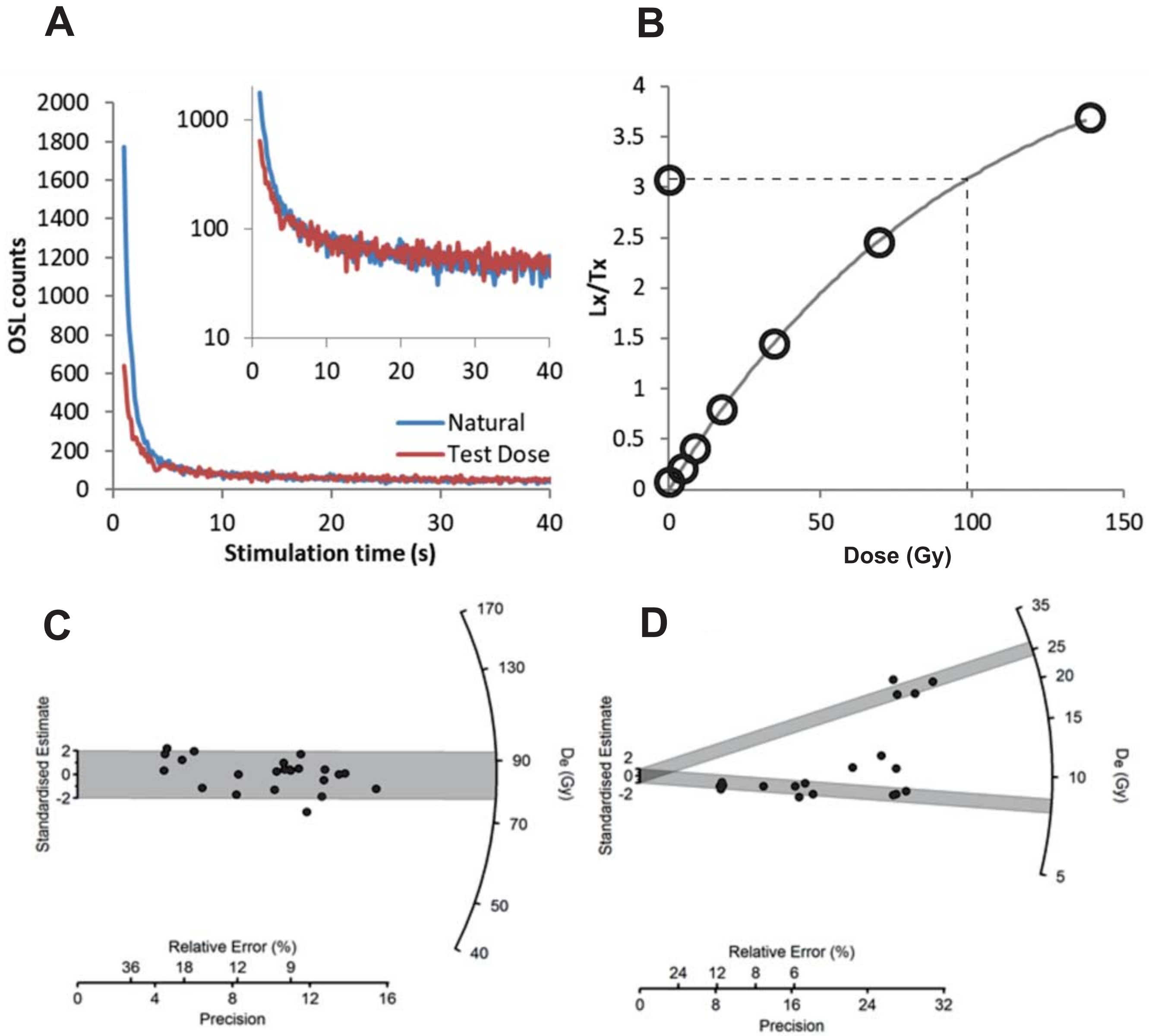

A
OSL counts
Stimulation time (s)
Natural
Test Dose
B
Lx/Tx
Dose (Gy)
C
Standardised Estimate
De (Gy)
Relative Error (%)
Precision
D
Standardised Estimate
De (Gy)
Relative Error (%)
Precision

Figure 7

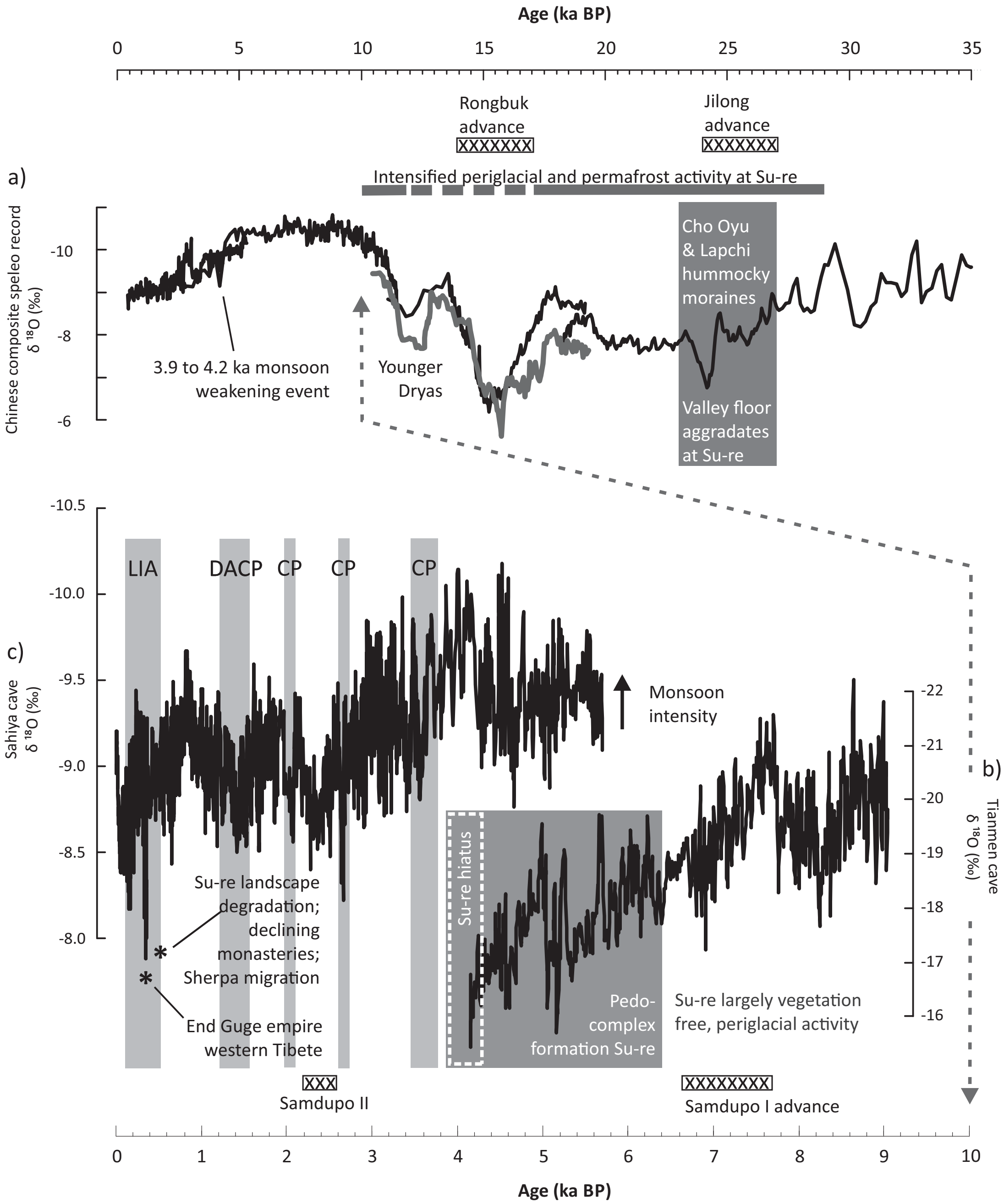
Age (ka BP)
0 5 10 15 20 25 30 35
Rongbuk advance
XXXXXXX
Jilong advance
XXXXXXX
a)
Intensified periglacial and permafrost activity at Su-re
Chinese composite speleo record δ 18O (‰)
-10
-8
-6
Cho Oyu & Lapchi hummocky moraines
Valley floor aggradates at Su-re
3.9 to 4.2 ka monsoon weakening event
Younger Dryas
-10.5
-10.0
-9.5
-9.0
-8.5
-8.0
c)
Sahiya cave δ 18O (‰)
LIA
DACP
CP
CP
CP
Monsoon intensity
-22
-21
-20
-19
-18
-17
-16
b)
Tianmen cave δ 18O (‰)
Su-re hiatus
Su-re landscape degradation; declining monasteries; Sherpa migration
End Guge empire western Tibete
Pedo-complex formation Su-re
Su-re largely vegetation free, periglacial activity
XXX
Samdupo II
XXXXXXXX
Samdupo I advance
0 1 2 3 4 5 6 7 8 9 10
Age (ka BP)

Figure 8

Table 1: Radiocarbon samples from the archaeological site of Su-re and calibrated ages.

Sample code Fig 4 & text	Sample code	Latitude (X°)	Longitude (Y°)	depth[1] (cm)	Fraction dated[2]	Radicarbon Lab code[3]	uncal. BP[4] (yBP)	d13C (‰)[5]	d13C Source	F[6] [ ]	C[7] (mg)	C Yield (%)	yrs. cal. BP[8] (years cal. BP)
R1	TIN2016-14C-1	28.5150	86.6746	90	Sediment	CEDAD_n.n.							n.a.*
R4	TIN2016-14C-4	28.5150	86.6746	72	Sediment	Poz-99983	5200 ± 35	-25.1 ± 1.0	AMS	0.525 ± 0.002	0.2	0.3	5903-6168
R5	TIN2016-14C-5	28.5150	86.6746	60	Sediment	CEDAD_LTL16960A	5881 ± 50	-32.9 ± 0.6	AMS	0.481 ± 0.003	1.5	58	6562-6844
R5x	TIN2016-14C-5	28.5150	86.6746	60	Sediment	Poz-100148	3925 ± 30	-20.5 ± 0.3	AMS	0.614 ± 0.002	1.0	1.0	4249-4438**
R6	TIN2016-14C-6	28.5162	86.6704	53	Charcoal	CEDAD_LTL16961A	2792 ± 45	-23.5 ± 0.3	AMS	0.706 ± 0.004	0.3	<1	2781-3000***
R17	TIN2014-17	28.5241	86.6641	130	Sediment	Poz-71933	5560 ± 40	-29.4 ± 1.0	AMS	0.501 ± 0.002	1.4	0.6	6289-6411

(1) Refers to depth below surface in stratigraphic profile (Figure 4)

(2) Sediment refers to organic rich sediment horizons detailed in text

(3) Radiocarbon Laboratory codes: CEDAD = Centro di Datazione e Diagnostica, Univeristy del Salento, Italy; Poz = Poznan Radiocarbon Laboratory, Poland

(4) Uncalibrated years before present (BP; ie. before 1950) is the conventional radiocarbon age as defined by Stuiver and Polach, (1977)

(5) $\delta^{13}C$ normalization is performed using δ13C measured by AMS, thus accounting for AMS fractionation

(6) Fraction modern (F) is the blank corrected fraction modern normalized to $\delta^{13}C$ of -25‰, defined by Donahue et al. (1990).

(7) Carbon dioxide was generated by sealed combustion at 900°C in vacuum sealed quartz tubes to obtain the graphite target (C) reported in mg

(8) Calibrated with IntCal13 (Stuiver, M., Reimer, P.J., and Reimer, R.W., 2019, CALIB 7.1 [WWW program] at http://calib.org, accessed 2019-2-191993); Calibrated ages are reported at 95% probablity (2σ).

Where two age ranges are given we report the full span. Note that in the text and in Figure 4 the ages are reported as thousand years (ka) cal. BP

* Not enough C yield, hence undateable

** Replicate sample of sample R5, but without floatation treatment, hence modern rootlet contamination probably caused observed age underestimation

*** Due to the very low carbon yield this age is regarded as unreliable and omitted from the sediment logs in Figure 4

Table 2: Environmental dose (De) values, dose rates and age data for coarse grained sediment samples from Su-re. See text for discussion of two italicized ages.

Sample	Sed log (Fig 4)	Latitude (X°)	Longitude (Y°)	Depth (cm)	Aliquots (n)	Age model	De (Gy)	Overdispersion (%)	Gamma dose rate (Gy/ka)	Beta dose rate (Gy/ka)	Cosmic dose rate (Gy/ka)	Internal dose rate (Gy/ka)	Total dose rate* (Gy/ka)	Age (ka)
TIN 5x	R-1	28.5129	86.6700	96	24	CAM	44.8 ± 1.8	14 ± 4	1.38 ± 0.03	2.20 ± 0.10	0.44 ± 0.04	0.03 ± 0.01	4.04 ± 0.18	11.07 ± 0.70
TIN 5	Bo-110	28.5124	86.6753	251	23	CAM	2.65 ± 0.2	16 ± 6	1.77 ± 0.04	2.40 ± 0.11	0.36 ± 0.04	0.03 ± 0.01	4.57 ± 0.20	0.58 ± 0.04
TIN 6	Bo-110	28.5124	86.6753	77	17	CAM	2.90 ± 0.4	40 ± 12	1.61 ± 0.03	2.45 ± 0.10	0.45 ± 0.04	0.03 ± 0.01	4.55 ± 0.19	0.64 ± 0.09
TIN 8	R-3	28.5108	86.6775	160	23	CAM	85 ± 2.2	7 ± 3	1.61 ± 0.03	2.48 ± 0.11	0.41 ± 0.04	0.03 ± 0.01	4.54 ± 0.19	18.72 ± 1.01
TIN 9	Pit-H	28.5167	86.6702	115	16	CAM	128 ± 5.1	7 ± 6	1.73 ± 0.04	2.63 ± 0.11	0.43 ± 0.04	0.03 ± 0.01	4.82 ± 0.21	26.62 ± 1.65
TIN 10	Pit-H	28.5167	86.6702	75	22	CAM	84 ± 2.1	0 ± 0	1.58 ± 0.03	2.51 ± 0.11	0.45 ± 0.04	0.03 ± 0.01	4.57 ± 0.20	18.43 ± 1.00
TIN 11	Pit-H	28.5167	86.6702	45	22	CAM	23.5 ± 1.1	17 ± 4	2.18 ± 0.05	3.09 ± 0.14	0.47 ± 0.05	0.03 ± 0.01	5.77 ± 0.25	4.07 ± 0.27
TIN 12	G-2A	28.5165	86.6668	48	24	CAM	3.4 ± 0.4	45 ± 10	2.07 ± 0.05	2.94 ± 0.13	0.47 ± 0.05	0.03 ± 0.01	5.51 ± 0.24	0.61 ± 0.08
TIN 13**	G-2A	28.5165	86.6668	77	22	CAM	22 ± 2.0	40 ± 7	2.24 ± 0.06	3.00 ± 0.13	0.45 ± 0.04	0.03 ± 0.01	5.72 ± 0.25	3.88 ± 0.42
					2	CAM high De	59 ± 6.7							*10.34 ± 1.27*
					20	CAM low De	20 ± 1.2							3.49 ± 0.27
TIN 14	R-4	28.5129	86.6717	135	22	CAM	105 ± 4.2	9 ± 5	1.44 ± 0.03	2.20 ± 0.10	0.42 ± 0.04	0.03 ± 0.01	4.08 ± 0.18	25.72 ± 1.59
TIN 15	Tv-1	28.5240	86.6637	40	22	CAM	59 ± 3.1	11 ± 8	2.00 ± 0.04	2.90 ± 0.13	0.47 ± 0.05	0.03 ± 0.01	5.41 ± 0.23	10.90 ± 0.78
TIN 16	Tv-3	28.5241	86.6640	130	22	CAM	2.7 ± 0.3	35 ± 11	1.67 ± 0.04	2.63 ± 0.11	0.42 ± 0.04	0.03 ± 0.01	4.75 ± 0.21	0.56 ± 0.07
TIN 19	Pit-H	28.5167	86.6702	60	23	CAM	2.0 ± 0.2	46 ± 9	1.55 ± 0.03	2.55 ± 0.11	0.46 ± 0.05	0.03 ± 0.01	4.59 ± 0.20	0.44 ± 0.05
TIN 1y	Pit-01	28.5166	86.6700	30	19	CAM	115 ± 6.6	21 ± 5	1.49 ± 0.03	2.41 ± 0.11	0.48 ± 0.05	0.03 ± 0.01	4.41 ± 0.19	26.18 ± 1.95
TIN 2y	Pit-01	28.5166	86.6700	41	23	CAM	105 ± 4.4	16 ± 4	1.53 ± 0.03	2.46 ± 0.11	0.47 ± 0.05	0.03 ± 0.01	4.49 ± 0.20	23.43 ± 1.48
TIN 3y	F-1	28.6746	86.6717	81	24	CAM	46 ± 2.2	21 ± 4	1.52 ± 0.03	2.22 ± 0.10	0.45 ± 0.04	0.03 ± 0.01	4.21 ± 0.18	10.95 ± 0.74
TIN 4y**	F-1	28.6746	86.6717	30	21	CAM	25.3 ± 1.1	48 ± 8	1.84 ± 0.04	2.81 ± 0.12	0.48 ± 0.05	0.03 ± 0.01	5.16 ± 0.22	1.94 ± 0.23
					4	CAM high De	25.3 ± 1.1							4.90 ± 0.32
					17	CAM low De	8.1 ± 0.4							*1.57 ± 0.11*
TIN 5y	G-1A	28.6762	86.6704	105	22		66 ± 2.6	15 ± 4	1.68 ± 0.04	2.56 ± 0.11	0.43 ± 0.04	0.03 ± 0.01	4.70 ± 0.20	14.03 ± 0.87
TIN 6y	G-1A	28.6762	86.6704	57	22		37.7 ± 1.8	21 ± 4	2.32 ± 0.05	3.11 ± 0.14	0.46 ± 0.05	0.03 ± 0.01	5.92 ± 0.25	6.38 ± 0.43

* Includes an internal contribution of 0.03±0.01 Gy/ka

** Contains two apperant dose populations (high and low De population, respectively. Hence, the CAM De values and ages for entire dataset (all aliquots) and high and low De populations are provided.

Table 3: Dose rates and feldspar luminescence ages based on the post-IR IRSL 290 signal for four pottery sherds from Su-re.

Sample	Latitude (X°)	Longitude (Y°)	Depth (cm)	Moisture content (%)	Sherd alpha (Gy/ka)	Sherd beta (Gy/ka)	Sherd gamma (Gy/ka)	Sediment Gamma (Gy/ka)	Cosmic Dose (Gy/ka)	Total dose rate (Gy/ka)	De (Gy)	Age (ka)
TIN28	28.5134	86.6715	0	2 ± 2	1.49 ± 0.30	3.20 ± 0.19	2.10 ± 0.04	2.14 ± 0.05	0.42 ± 0.04	6.20 ± 0.36	3.07 ± 0.23	0.50 ± 0.05
TIN22	28.5129	86.6705	40	2 ± 2	1.49 ± 0.30	3.20 ± 0.19	2.10 ± 0.04	2.14 ± 0.05	0.40 ± 0.04	7.22 ± 0.37	6.24 ± 0.15	0.86 ± 0.05
TIN23a	28.5129	86.6705	40	2 ± 2	1.49 ± 0.30	3.20 ± 0.19	2.10 ± 0.04	2.14 ± 0.05	0.40 ± 0.04	7.22 ± 0.37	5.27 ± 0.15	0.73 ± 0.05
TIN23b	28.5129	86.6705	40	2 ± 2	1.49 ± 0.30	3.20 ± 0.19	2.10 ± 0.04	2.14 ± 0.05	0.40 ± 0.04	7.22 ± 0.37	5.67 ± 0.15	0.78 ± 0.05

Table 4: Cosmogenic radionuclide concentrations and ages for five moraine boulders from the Cho Oyu hummocky moraine. All samples were treated with in-house ^{9}Be carrier (Merchel et al., 2013). No geographical shielding corrections were necessary.

Sample ID	Lab number (Be)	Lab number (Al)	Latitude °X	Longitude °Y	Altitude (m asl)	Sample thickness (cm)	Quartz mass (g)	^{9}Be addition (mg)	Al [(1)] (µg/g)	^{10}Be/^{9}Be [(2)] (10^{-12})	^{26}Al/^{27}Al [(2)] (10^{-12})	^{10}Be [(3)] (10^{6} at/g)	^{26}Al [(3)] (10^{6} at/g)	^{10}Be age [(5)] (ka)	^{26}Al age [(5)] (ka)	^{26}Al/^{10}Be [(6)]
Oyu_126	B2140	A0687	28.3979	86.6352	4690	3	19.115	0.3162	1612	1.167 ± 0.085[(3)]	0.0542 ± 0.0045	1.288 ± 0.094	1.93 ± 0.17	19.9 ± 2.2	4.85 ± 0.60	1.7 ± 0.2
Oyu_127	B2141	A0688	28.3971	86.6340	4690	3	17.935	0.3165	551	0.735 ± 0.018	0.272 ± 0.011	0.865 ± 0.021	3.32 ± 0.17	13.3 ± 1.2	8.37 ± 0.84	4.3 ± 0.2
Oyu_128	B1843	A0581	28.3961	86.6395	4690	3	29.164	0.3166	1219	1.056 ± 0.075[(3)]	0.250 ± 0.015	0.763 ± 0.054	6.80 ± 0.45	11.8 ± 1.3	17.2 ± 1.9	9.9 ± 1
Oyu_129	B1844	A0582	28.3971	86.6385	4690	3	49.467	0.3164	116	4.040 ± 0.079	2.926 ± 0.075	1.726 ± 0.034	7.56 ± 0.30	26.7 ± 2.4	19.2 ± 1.8	4.8 ± 0.2
Oyu_131	B1845	A0583	28.3961	86.6352	4690	3	49.372	0.3170	680	2.41 ± 0.14[(3)]	0.241 ± 0.017	1.032 ± 0.061	3.67 ± 0.29	15.9 ± 1.7	9.3 ± 1.1	3.9 ± 0.4

(1) Measured by ICP-MS. Uncertainties are 3%.

(2) Not blank-corrected. Uncertainties are AMS analytical uncertainties, i.e., the larger of counting statistics and the spread of repeated measurements, standard normalisation, but no blank corrections.

(3) Overall uncertainties have been doubled as samples did contain unreasonable amounts of Ti- and Al-oxides (originating from non-pure quartz dissolved) reducing the ^{9}Be current to only 2.9-4.6% compared to the standard.

(4) Uncertainties include in quadrature, AMS analytical uncertainties, standard uncertainty (1.76% for ^{10}Be/^{9}Be and 1.46% for ^{26}Al/^{27}Al) and reproducibility, blank corrections and stable ^{27}Al measurements.

(5) Exposure ages were calculated by CRONUS Earth (Balco et al. 2008), assuming zero-erosion (version: wrapper script 2.3, main calulator 2.1, constants 2.3, muons 1.1). Errors are 'external uncertainty'. Production rates are based on Lal (1991)/Stone (2000) are 0.290 at/g/yr (muons) and 58.62 at/g/yr (spallation) for ^{10}Be, and 2.881 at/g/yr (muons) and 395.49 at/g/yr (spallation) for ^{26}Al.

(6) relative to 07KNSTD

Table 5: Morphometrics of inferred sling shot projectiles and hammer stones (compare Figure 3 for distribution of these artefacts in landscape)

Sample	Latitude (X°)	Longitude (Y°)	Shape	a-axis diameter (cm)	Mass (kg)	Clast morphology	Broken surface	Embedding
006	28.5155	86.6746	spherical	5	1.0	rounded		semi-embedded
007	28.5158	86.6746	spherical	4	0.5	well rounded		semi-embedded
011	28.5165	86.6714	spherical	4	0.5	well rounded		surface find
012	28.5165	86.6710	disc-shaped	6	1.0	rounded		surface find
013	28.5166	86.6703	bladed	13	10.3	well rounded		semi-embedded
014	28.5166	86.6707	spherical	5	1.0	well rounded		semi-embedded
015	28.5166	86.6705	spherical	5	1.0	well rounded	x	surface find
016	28.5166	86.6705	disc-shaped	7	1.6	rounded		surface find
017a	28.5165	86.6702	bladed	7	1.6	rounded	x	semi-embedded
017b	28.5166	86.6701	spherical	4	0.5	rounded	x	semi-embedded
018	28.5165	86.6702	disc-shaped	n.a.[1]	n.a.[1]	rounded	x	surface find
019	28.5164	86.6702	spherical	6	1.7	well rounded		semi-embedded
020	28.5162	86.6702	bladed	8	2.4	well rounded	x	surface find
021	28.5161	86.6703	bladed	7	1.6	angular	x	surface find
022	28.5162	86.6704	spherical	4.5	0.7	rounded	x	surface find
023	28.5163	86.6703	spherical	5	1.0	well rounded		semi-embedded
099	28.5178	86.6696	spherical	4	0.5	well rounded		surface find

[1]clast broken on two sides, orignal size and mass unknown

Re-submission of the manuscript:

Landscape dynamics and human-environment interactions in the northern foothills of Cho Oyu and Mount Everest (southern Tibet) during the Late Pleistocene and Holocene

Meyer, M. C.*; Gliganic, L. A.; May, J-H.; Merchel, S.; Rugel, G. ; Schlütz, F.; Aldenderfer, M. S. and Krainer, K.

*corresponding author

Dear Editor,

We have no conflict of interest

Yours sincerely,

M. Meyer and co-authors

References

Aitken, M.J., 1985. Thermoluminescence Dating. Academic Press, London.

Aitken, M.J., 1998. An Introduction to Optical Dating: The Dating of Quaternary Sediments by the Use of Photon-stimulated Luminescence. Oxford University Press, Oxford.

Akhmadaliev, S., Heller, R., Hanf, D., Rugel, G., Merchel, S. 2013. The new 6 MV AMS-facility DREAMS at Dresden, Nucl. Instr. Meth. Phys. Res. B 294, 5–10.

Aldenderfer, M. 2011. Peopling the Tibetan Plateau: Insights from archaeology. High Altitude Med. & Biol. 12, 141-147.

Aldenderfer, M. and Yinong, Z. 2004. The prehistory of the Tibetian Plateau to the Seventh Century A.D.: Perspectives and Research from China and the West since 1950. Journal of World Prehistory 18, 1-55.

Armijo, R., Tapponnier, P., Mercier, J.L. and Han, T.-L. 1986. Quaternary extension in southern Tibet: Field observations and tectonic implications. Journal of Geophysical Research: Solid Earth 91 (B14): 13803-13872.

Balco G, Stone J.O, Lifton N.A., Dunai T.J., 2008. A complete and easily accessible means of calculating surface exposure ages or erosion rates from 10Be and ^{26}Al measurements. Quaternary Geochronology 3, 174–195.

Barker, S., Knorr, G., Edwards, R.L., Parrenin, F., Putnam, A.E., Skinner, L.C., Wolff, E. and Ziegler, M., 2011. 800,000 years of abrupt climate variability. Science 334(6054), 347-351.

Barsch, D. 1992. Permafrost creep and rock glaciers. Permafrost and Periglacial Processes, 3, 175-188.

Barsch D. 1996. Rockglaciers: Indicators for the Present and Former Geoecology in High Mountain Environments. Springer: Berlin, Heidelberg.

Bateman, M.D., Thomas, D.S.G., Singhvi, A.K., 2003. Extending the aridity record of the southwest Kalahari: current problems and future perspectives. Quat. Int. 111, 37–49.

Benn, D.I. and Owen, L.A., 2002. Himalayan glacial sedimentary environments: a framework for reconstructing and dating the former extent of glaciers in high mountains. Quaternary International 97 - 98, 3-25.

Benn, D.I., Kirkbride, M.P., Owen, L.A. and Brazier, V., 2003. Glaciated valley landsystems. Glacial landsystems. In: Evans, D.J.A. (Ed.), Glacial Landsystems. Arnold, London. pp.372-406.

Bhandari, S., Zhang, X., Cui, C., , B., Liao, S., Peng, Y., Zhang, H., Xiang, K., Shi, H., , O., , B., , G., Liu, S., , G., Wu, T., Qi, X. and Su, B., 2015. Genetic evidence of a recent Tibetan ancestry to Sherpas in the Himalayan region. Scientific Reports 5, 16249.

Bird, B.W., Polisar, P.J., Lei, Y., Thompson, L.G., Yao, T., Finney, B.P., Bain, D.J., Pompeani, D.P. and Steinman, B.A., 2014. A Tibetan lake sediment record of Holocene Indian summer monsoon variability. Earth and Planetary Science Letters 399, 92-102.

Blöthe, J.H., Rosenwinkel, S., Höser, T. and Korup, O., 2019. Rock-glacier dams in High Asia. Earth Surface Processes and Landforms, 44(3), pp.808-824.

Bookhagen, B. and Burbank, D.W. 2010. Toward a complete Himalayan hydrological budget: Spatiotemporal distribution of snowmelt and rainfall and their impact on river discharge. Journal of Geophysical Research: Earth Surface 115 (F3):

Bookhagen, R. and Burbank, D.W., 2006. Topography, relief, and TRMM-derived rainfall variations along the Himalaya. Geophysical Research Letters 33, L08405, doi:10.1029/2006GL026037.

Bøtter-Jensen, L., Andersen, C.E., Duller, G.A.T., Murray, A.S., 2003. Developments in radiation, stimulation and observation facilities in luminescence measurements. Radiat. Meas. 37 (4-5), 535-541.

Bøtter-Jensen, L., Mejdahl, V., 1988. Assessment of beta dose-rate using a GM multicounter system.

Nuclear Tracks and Radiation Measurements 14, 187–191.

Brock, F., Higham, T., Ditchfield, P., Bronk Ramsey, C., 2010. Current pretreatment methods for AMS radiocarbon dating at the Oxford Radiocarbon Accelerator (ORAU). Radiocarbon 52, 103–112.

Brown, E.T., Edmond, J.M., Raisbeck, G.M., Yiou, F., Kurz, M.D., Brook, E.J., 1991. Examination of surface exposure ages of Antarctic moraines using in situ produced ^{10}Be and ^{26}Al, Geochim. Cosmochim. Acta 55, 2269–2283.

Burchfiel, B. C., Chen, Z., Hodges, K. V., Liu, Y., Royden, L. H., Deng, C., and Xu, J. 1992. The South Tibetan detachment system, Himalayan Orogen: extension contemporaneous with and parallel to shortening in a collisional mountain belt. Boulder, CO, Geological Society of America 41 p.yers, A., 2005. Contemporary human impacts on Alpine ecosystems in the Sagarmatha (Mt. Everest) national park, Khumbu, Nepal. Annals of the association of American Geographers 95, 112-140.

Cai, Y., Cheng, H., An, Z., Edwards, R.L., Wang, X., Tan, L. and Wang, J. 2010. Large variations of oxygen isotopes in precipitation over south-central Tibet during Marine Isotope Stage 5. Geology 38, 243-246.

Cai, Y., Fung, I.Y., Edwards, R.L., Ana, Z., Chen, H., Lee, J.-E., Tan, L., Shen, C.-C., Wang, X., Day, J.A., Zhou, W., Kelly, M.J. and Chian, J.C.H., 2015. Variability of stalagmite-inferred Indian monsoon precipitation over the past 252,000 y. PNAS 112, 2954-2959.

Cai, Y., Haiwei, Z., Hai, C., Zhisheng, A., Lawrence, E.R., Xianfeng, W., Liangcheng, T., Fuyuan, L., Jin, W. and Megan, K. 2012. The Holocene Indian monsoon variability over the southern Tibetan Plateau and its teleconnections. Earth and Planetary Science Letters 335, 135-144.

Cheng, G. and Wu, T. 2007. Responses of permafrost to climate change and their environmental significance, Qinghai-Tibet Plateau. Journal of Geophysical Research: Earth Surface, 112(F2).

Cheng, H., Edwards, R.L., Broecker, W.S., Denton, G.H., Kong, X., Wang, Y., Zhang, R. and Wang, X., 2009. Ice age terminations. Science 326 (5950), 248-252.

Cheng, H., Edwards, R.L., Sinha, A., Spötl, C., Yi, L., Chen, S., Kelly, M., Kathayat, G., Wang, X., Li, X., Kong, X., Wang, Y., Ning, Y. and Zhang, H. 2016. The Asian monsoon over the past 640,000 years and ice age terminations. Nature 534, 640-646.

Cheng, H., Sinha, A., Wang, X., Cruz, F.W. and Edwards, R.L., 2012. The Global Paleomonsoon as seen through speleothem records from Asia and the Americas. Climate Dynamics, 39, 1045-1062.

Chevalier, M.-L., Hilley, G., Tapponnier, P., Van Der Woerd, J., Liu-Zeng, J., Finkel, R.C., Ryerson, F.J., Li, H. and Liu, X., 2011. Constraints on the late Quaternary glaciations in Tibet from cosmogenic exposure ages of moraine surfaces. Quaternary Science Reviews 30, 528-554.

Church, M., Stock, R. F., & Ryder, J. M., 1979. Contemporary sedimentary environments on Baffin Island, NWT, Canada: debris slope accumulations. Arctic and Alpine Research 11, 371-401.

Clark, P.U., Dyke, A.S., Shakun, J.D., Carlson, A.E., Clark, J., Wohlfarth, B., Mitrovica, J.X., Hostetler, S.W. and McCabe, A.M., (2009): The last glacial maximum. Science 325, 710-714.

Conroy, J.L., Hudson, A.M., Overpeck, J.T., Liu, K.-B., Wang, L. and Cole, J.E., 2017. The primacy of multidecadal to centennial variability over late-Holocene forced change of the Asian Monsoon on the southern Tibetan Plateau. Earth and Planetary Science Letters 458, 337-348.

Cremonese, E., Gruber, S., Phillips, M., Pogliotti, P., Böckli, L., Noetzli, J., Suter, C., Bodin, X., Crepaz, A., Kellerer-Pirklbauer, A. and Lang, K., 2011. An inventory of permafrost evidence for the European Alps. The Cryosphere, 5, 651-657.

Cunningham, A.C., Wallinga, J., 2010. Selection of integration time intervals for quartz OSL decay curves. Quat. Geochronol. 5, 657–666.

De Keyzer, M. and Bateman, M.D., 2018. Late Holocene landscape instability in the Breckland (England) drift sands. Geomorphology 323. 123-134.

D'Elia, M., Calcagnile, L., Quarta, G., Sanapo, C., Laudisa, M., Toma, U., Rizzo, A., 2004. Sample preparation and blank values at the AMS radiocarbon facility of the University of Lecce Nuclear Instruments and Methods in Physics Research, Section B: Beam Interactions with Materials and Atoms, 223-224 (SPEC. ISS.), 278-283. DOI: 10.1016/j.nimb.2004.04.056

Dixit, Y., Hodell, D.A., Sinha, R. and Petrie, C.A., 2014. Abrupt weakening of the Indian summer monsoon at 8.2 kyr B.P. Earth and Planetary Science Letters 391, 16-23.

Donahue, D. J., Linick, T. W., Jull, A. J. T., 1990. Jull, Isotope-ratio and background corrections for accelerator mass spectrometry radiocarbon measurements. Radiocarbon 32, 135–142. doi:10.1017/S0033822200040121

Donges, J.F., Donner, R.V., Marwan, N., Breitenbach, S.F.M., Rehfeld, K. and Kurths, J., 2014. Nonlinear regime shifts in Holocene Asian monsoon variability: potential impacts on cultural change and migratory patterns. Climate of the Past 10, 895-975.

Duller, G.A.T., 2003. Distinguishing quartz and feldspar in single grain luminescence measurements. Radiat. Meas. 37 (2), 161-165.

Fleitmann, D., Burns, S.J., Mangini, A., Mudelsee, M., Kramers, J., Villa, I., Neff, U., Al-Subbary, A.A., Buettner, A., Hippler, D. and Matter, A., 2007. Holocene ITCZ and Indian monsoon dynamics recorded in stalagmites from Oman and Yemen (Socotra). Quaternary Science Reviews 26, 170-188.

Fleitmann, D., Burns, S.J., Mangini, A., Mudelsee, M., Kramers, J., Villa, I., Neff, U., Al-Subbary, A.A., Buettner, A., Hippler, D. and Matter, A., 2007. Holocene ITCZ and Indian monsoon dynamics recorded in stalagmites from Oman and Yemen (Socotra). Quaternary Science Reviews 26, 170-188.

French H. M., 2007. The periglacial environment. 3rd edition, Wiley,& Sons, West Sussex, England, UK, 458 pp.

French, H. and Thorn, C.E., 2006. The changing nature of periglacial geomorphology. Géomorphologie: relief, processus, environnement, 12, DOI : 10.4000/geomorphologie.119

French, H.M. and Bjornson, J.E.A.N., 2008. Mountain-top detritus and patterned ground in the Gaspésie Mountains, Québec, Canada. Geographia Polonica 8, 29-39.

Galbraith, R.F. and Roberts, R.G., 2012. Statistical aspects of equivalent dose and error calculation and display in OSL dating: An overview and some recommendations. Quaternary Geochronology 11 1-27.

Galbraith, R.F., Roberts, R.G., Laslett, G.M., Yoshida, H., Olley, J.M., 1999. Optical dating of single and multiple grains of quartz from Jinmium rock shelter, northern Australia: part I, experimental design and statistical models. Archaeometry 41, 339-364.

Gautama, R. and Thapa-Magar, A.K., 1994. Tribal ethnography of Nepal (vol. 2). Book Faith India.

Gliganic, L.A., May, J.-H., Cohen, T.J., 2015. All mixed up: using single-grain equivalent dose distributions to identify phases of pedogenic mixing on a dryland alluvial fan. Quat. Int. 362, 23e33.

Gliganic, L.A., Meyer, M.C., Sohbati, R., Jain, M. and Barrett, S., 2019. OSL surface exposure dating of a lithic quarry in Tibet: Laboratory validation and application. Quaternary Geochronology 49, 199-204.

Goswami, B.N. and Chakravorty, S., 2017. Dynamics of the Indian summer monsoon climate. Oxford Research Encyclopedia of Climate Science, p.38.

Guerin, G., Mercier, N., Adamiec, G., 2011. Dose-rate conversion factors: update. Ancient TL. 29, 5-8.

Haeberli, W. and Vonder Mühll, D., 1996. On the characteristics and possible origins of ice in rock glacier permafrost. Zeitschrift für Geomorphologie 104, 43-57.

Haeberli, W., 1983. Permafrost-glacier relationships in the Swiss Alps-today and in the past. In Proceedings of the Fourth International Conference on Permafrost, 1983 (pp. 415-420). National Academy Press.

Haeberli, W., Hallet, B., Arenson, L., Elconin, R., Humlum, O., Kääb, A., Kaufmann, V., Ladanyi, B., Matsuoka, N. and Springman, S., 2006. Permafrost creep and rock glacier dynamics. Permafrost and periglacial processes 17, 189-214.

Herzschuh, U., Ni, J., Birks, H.J.B. and Böhner, J., 2011. Driving forces of mid-Holocene vegetation shifts on the upper Tibetan Plateau, with emphasis on changes in atmospheric CO_2 concentrations. Quaternary Science Reviews 30, 1907-1917.

Heyman, J., 2014. Paleoglaciation of the Tibetan Plateau and surrounding mountains based on exposure ages and ELA depression estimates. Quaternary Science Reviews, 91, 30-41.Heyman, J., Stroeven, A. P., Harbor, J. M., & Caffee, M. W., 2011. Too young or too old: evaluating cosmogenic exposure dating based on an analysis of compiled boulder exposure ages. Earth and Planetary Science Letters 302, 71-80.

Hoke, L., Lamb, S., Hilton, D. R., and Podera, R. J., 2000. Southern limit of mantle-derived geothermal helium emissions in Tibet: implications for lithospheric structure. Earth Planet. Sci. Lett. 180, 297–208.

Hudson, A.M. and Quade, J., 2013. Long-term east-west asymmetry in monsoon rainfall on the Tibetan Plateau. Geology 41, 351-354.

Hudson, A.M. and Quade, J., 2013. Long-term east-west asymmetry in monsoon rainfall on the Tibetan Plateau. Geology 41, 351-354.

Hudson, A.M., Olsen, J.W., Quade, J., Lei, G., Huth, T.E. and Zhang, H., 2016. A regional record of expanded Holocene wetlands and prehistoric human occupation from paleowetland deposits of the western Yarlung Tsangpo valley, southern Tibetan Plateau. Quaternary Research 86, 13-33.

Hudson, A.M., Quade, J., Huth, T.E., Lei, G., Cheng, H., Edwards, L.R., Olsen, J.W. and Zhang, H., 2015. Lake level reconstruction for 12.8-2.3ka of the Ngangla Ring Tso closed-basin lake system, southwest Tibetan Plateau. Quaternary Research 83, 66-79.

Hummel, S. and Vogliotti, G., 2000. The Sling and the Inflated Skin Boat in Tibet. The Tibet Journal 25/3, 14-18. stable URL: http://www.jstor.org/stable/43302454 (Accessed: 12th August 2019).

Huntley, D.J., Godfrey-Smith, D.I., Thewalt, M.L.W., 1985. Optical dating of sediments. Nature 313, 105-107

Huth, T., Hudson, A.M., Quade, J., Guoliang, L. and Hucai, Z., 2015. Constraints on paleoclimate from 11.5 to 5.0 ka from shoreline dating and hydrologic budget modeling of Baqan Tso, southwestern Tibetan Plateau. Quaternary research 83, 80-93.

Ishikawa, M., Watanabe, T. and Nakamura, N., 2001. Genetic differences of rock glaciers and the discontinuous mountain permafrost zone in the Kanchanjung Himal, E Nepal. Permafrost and Periglacial Processes 12, 243-253.

Iwata, S., 1987. Debris-mantled rectilinear slopes in the western Sor Rondane Mountains, East Antarctica. Proceedings of the NIPR Symposium on Antarctic Geosciences 1, 178-192.

Jahn, A., 1984. Periglacial talus slopes. Geomorphological studies on Spitsbergen and in Northern Scandinavia. Polar Geography 8, 177-193.

Jessup, M.J. and Cottle, J.M., 2010. Progression from south-directed extrusion to orogen-parallel extension in the southern margin of the Tibetan Plateau, Mount Everest region, Tibet. The Journal of Geology 118, 467-486.

Jiang, T., Aitchison, J. C., & Wan, X., 2016. The youngest marine deposits preserved in southern Tibet and disappearance of the Tethyan Ocean. Gondwana Research 32, 64-75.

Jin, L., Schneider, B., Park, W., Latif, M., Khon, V. and Zhang, X., 2014. The spatial and temporal patterns of Asian summer monsoon precipitation in response to Holocene insolation change: a model-data synthesis. Quaternary Science Reviews 85, 47-62.

Johnson, C. G., Kokelaar, B. P., Iverson, R. M., Logan, M., LaHusen, R. G., & Gray, J. M. N. T., 2012. Grain-size segregation and levee formation in geophysical mass flows. Journal of Geophysical Research: Earth Surface, 117(F1).

Jones, D.B., Harrison, S., Anderson, K., Selley, H.L., Wood, J.L. and Betts, R.A., 2018. The distribution and hydrological significance of rock glaciers in the Nepalese Himalaya. Global and Planetary Change, 160, 123-142.

Joordens, C.A.J., d'Errico, F., Wesselingh, F.P., Munro, S., de Vos, J., Wallinga, J., Ankjaergaard, C., Reimann, T., Wijbrans, J.R., Kuiper, K.F., Mür, H.J., Coqueugniot, H., Prie, V., Joosten, I., van Os, B., Schulp, A.S., Panuel, M., van der Haas, V., Lustenhouwer, W., Reijmer, J.J.G., Roebroeks, W., 2015. Homo erectus at Trinil on Java used shells for tool production and engraving. Nature 518 , 228-231.

Kathayat, G., Cheng, H., Sinha, A., Spötl, C., Edwards, R.L., Zhang, H., Li, X., Yi, L., Ning, Y., Cai, Y. and Lui, W.L., 2016. Indian monsoon variability on millennial-orbital timescales. Scientific reports, 6, p.24374.

Kathayat, G., Cheng, H., Sinha, A., Yi, L., Li, X., Zhang, H., Li, H., Ning, Y. and Edwards, R.L., 2017. The Indian monsoon variability and civilization changes in the Indian subcontinent. Science Advances 3 (12), p.e1701296.

Kattel, D.B., Yao, T., Yang, W., Gao, Y. and Tian, L., 2015. Comparison of temperature lapse rates from the northern to the southern slopes of the Himalayas. International Journal of Climatology 35, 4431-4443.

King, O., Quincey, D.J., Carrivick, J.L. and Rowan, A.V., 2016. Spatial variability in mass change of glaciers in the Everest region, central Himalaya, between 2000 and 2015. The Cryosphere Discussions. 1-35. ISSN 1994-0432.

Kirchner, N., Greve, R., Stroeven, A.P. and Heyman, J., 2011. Paleoglaciological reconstructions for the Tibetan Plateau during the last glacial cycle: evaluating numerical ice sheet simulations driven by GCM-ensembles. Quaternary Science Reviews 30, 248-267.

Knudsen MF, Egholm, DL, Jansen JD., 2019. Time-integrating cosmogenic nuclide inventories under the influence of variable erosion, exposure, and sediment mixing. Quaternary Geochronology 51, 110-119.

Knudsen, M. F., & Egholm, D. L., 2018. Constraining Quaternary ice covers and erosion rates using cosmogenic 26Al/10Be nuclide concentrations. Quaternary Science Reviews 181, 65-75.

Kohl C.P., Nishiizumi K., 1992. Chemical isolation of quartz for measurement of in situ produced cosmogenic nuclides. Geochimica et Cosmochimica Acta 56, 3583–3587.

Konrad, S.K., Humphrey, N.F., Steig, E.J., Clark, D.H., Potter Jr, N. and Pfeffer, W.T., 1999. Rock glacier dynamics and paleoclimatic implications. Geology 27, 1131-1134.

Lal, D., 1991. Cosmic ray labeling of erosion surfaces: in situ nuclide production rates and erosion models. Earth and Planetary Science Letters, 104, 424-439.

Leighton, C.L., Thomas, D.S.G., Bailey, R.M., 2014. Reproducibility and utility of dune luminescence chronologies. Earth Sci. Rev. 129, 24–39.

Li, K., Liu, X., Herzschuh, U. and Wang, Y., 2016. Rapid climate fluctuations over the past millennium: evidence from a lacustrine record of Basomtso Lake, southeastern Tibetan Plateau. Scientific Reports 6, p.24806.

Lifton, N., Bieber, J., Clem, J., Duldig, M., Evenson, P., Humble, J., Pyle, R., 2005. Addressing solar modulation and long-term uncertainties in scaling secondary cosmic rays for in situ cosmogenic nuclide applications. Earth and Planetary Science Letters 239, 140-161.

Löffler, J., 2000. High mountain ecosystems and landscape degradation in northern Norway. Mountain Research and Development 20, 356-364.

Lu, H., Mason, J.A., Stevens, T., Zhou, Y., Yi, S., Miao, X., 2011. Response of surface processes to climatic change in the dunefields and loess plateau of north China during the late Quaternary. Earth Surf. Process. Landf. 36, 1590–1603.

Lungershausen, U., Larsen, A., Bork, H.-R. and Duttmann, R., 2018. Anthropogenic influence on rates of aeolian dune activity within the northern European Sand Belt and socio-economic feedbacks over the last~ 2500 years. The Holocene 28, 84-103.

Maizels, J.K., 1979. Proglacial Aggradation and changes in braided channel patterns during a period of glacier advance: an alpine example. Geografiska Annaler 61 A, 87-101.

Matsuoka, N., Hirakawa, K., Watanabe, T., & Moriwaki, K., 1997. Monitoring of periglacial slope processes in the Swiss Alps: the first two years of frost shattering, heave and creep. Permafrost and Periglacial Processes 8, 155-177.

Matthews, J.A. and Briffa, K.R., 2005. The Little Ice Age: re-evaluation of an evolving concept. Geografiska Annaler: Series A, Physical Geography 87, 17-36.

Maussion, F., Scherer, D., Mölg, T., Collier, E., Curio, J. and Finkelnburg, R., 2014. Precipitation seasonality and variability over the Tibetan Plateau as resolved by the High Asia Reanalysis. Journal of Climate 27, 1910-1927.

Merchel, S., Bremser, W., 2004. First international ^{26}Al interlaboratory comparison - Part I, Nucl. Instr. Meth. Phys. Res. B 223-224, 393–400.

Merchel, S., Bremser, W., Bourles, D.L., Czeslik, U., Erzinger, J., Kummer, N.A., Leanni, L., Merkel, B., Recknagel, S. and Schaefer, U., 2013. Accuracy of ^{9}Be-data and its influence on ^{10}Be cosmogenic nuclide data. Journal of Radioanalytical and Nuclear Chemistry 298, 1871-1878.

Merchel, S., Bremser, W., Bourlès, D.L., Czeslik, U., Erzinger, J., Kummer, N.-A., Leanni, L., Merkel, B., Recknagel, S., Schäfer, U., 2013. Accuracy of 9Be-data and its influence on ^{10}Be cosmogenic nuclide data, J. Radioanal. Nucl. Chem. 298, 1871–1878.

Merchel, S., Herpers, U., 1999. An Update on Radiochemical Separation Techniques for the Determination of Long-Lived Radionuclides via Accelerator Mass Spectrometry, Radiochim. Acta 84, 215–219.

Meyer, M.C., Aldenderfer, M.S., Wang, Z., Hoffmann, D.L., Dahl, J.A., Degering, D., Haas, W.R. and Schlütz, F., 2017. Permanent human occupation of the central Tibetan Plateau in the early Holocene. Science 355 (6320), 64-67.

Meyer, M.C., Gliganic, L.A., Jain, M., Sohbati, R. and Schmidmair, D., 2018. Lithological controls on light penetration into rock surfaces implications for OSL and IRSL surface exposure dating. Radiation Measurements 120, 298-304.

Miehe, G., Miehe, S., Böhner, J., Kaiser, K., Hensen, I., Madsen,D., Liu, J. and Opgenoorth, L., 2014. How old is the human footprint in the world's largest alpine ecosystem? A review of multiproxy records from the Tibetan Plateau from the ecologists' viewpoint. Quaternary Science Reviews 86, 190-209.

Mitchell, W. A., & Taylor, P. J., 2001. Rock glaciers in the northwestern Indian Himalaya. Glacial Geology and Geomorphology rp01, 1-26.

Morrill, C., Overpeck, J.T. and Cole, J.E., 2003. A synthesis of abrupt changes in the Asian summer monsoon since the last deglaciation. The Holocene 13´, 465-476.

Mügler, I., Gleixner, G., Günther, F., Mäusbacher, R., Daut, G., Sch++tt, B., Berking, J., Schwalb, A., Schwark, L. and Xu, B., 2010. A multi-proxy approach to reconstruct hydrological changes and Holocene climate development of Nam Co, Central Tibet. Journal of Paleolimnology 43, 625-648.

Murray, A.S., Wintle, A.G., 2000. Luminescence dating of quartz using an improved single- aliquot regenerative-dose protocol. Radiat. Meas. 32, 57-73.

Murray, A.S., Wintle, A.G., 2003. The single aliquot regenerative dose protocol : potential for improvements in reliability. Radiat. Meas. 37, 377-381

Newell, D. L., Jessup, M. J., Cottle, J. M., Hilton, D. R., Sharp, Z., and Fischer, T., 2008. Aqueous and isotope geochemistry of mineral springs along the southern margin of the Tibetan plateau: implications for fluid sources and regional degassing of CO_2.Geochem. Geophys. Geosyst 9, Q08014.

Nishiizumi, K., Imamura, M., Caffee, M.W., Southon, J.R., Finkel, R.C., McAninch, J., 2007. Absolute calibration of 10Be AMS standards, Nucl. Instr. Meth. Phys. Res. B 258, 403–413.

Oppitz, M., 1974. Myths and facts: Reconsidering some data concerning the clan history of the Sherpas. The Sherpa Society 1, 121-131. http://www.dspace.cam.ac.uk/handle/1810/227209 (Accessed: 12th August 2019).

Owen, L.A. and England, J., 1998. Observations on rock glaciers in the Himalayas and Karakoram Mountains of northern Pakistan and India. Geomorphology 26, 199-213.

Owen, L.A., Benn, D.I., 2005. Equilibrium-line altitudes of the last glacial maximum for the Himalaya and Tibet: an assessment and evaluation of results. Quaternary International 138-139, 55-78.

Owen, L.A., Robinson, R., Benn, D.I., Finkel, R.C., Davis, N.K., Yi, C., Putkonen, J., Li, D. and Murray, A.S., 2009. Quaternary glaciation of Mount Everest. Quaternary Science Reviews 28, 1412-1433.

Pan, M., Wu, Y., Zheng, Y., Tan, L., 2014. Holocene aeolian activity in the Dinggye area (southern Tibet, China). Aeolian Res. 12, 19–27.

Pierik, H.J., van Lanen, R.J., Gouw-Bouman, M.T., Groenewoudt, B.J., Wallinga, J. and Hoek, W.Z., 2018. Controls on late-Holocene drift-sand dynamics: The dominant role of human pressure in the Netherlands. The Holocene 28, 1361-1381.

Prescott, J.R., Hutton, J.T., 1994. Cosmic ray contributions to dose rates for luminescence and ESR dating: large depths and long-term time variations. Radiat. Meas. 23 (1), 497-500.

Qi, W., Zhang, B., Yao, Y., Zhao, F., Zhang, S. and He, W., 2016. A topographical model for precipitation pattern in the Tibetan Plateau. Journal of Mountain Science 13, 763-773.

Rades, E.F., Hetzel, R., Xu, Q. and Ding, L., 2013. Constraining Holocene lake-level highstands on the Tibetan Plateau by 10Be exposure dating: a case study at Tangra Yumco, southern Tibet. Quaternary Science Reviews 82, 68-77.

Rapp, A., 1985. Extreme rainfall and rapid snowmelt as causes of mass movements in high latitude mountains. Field and Theory: Lectures in Geocryology, 36-56.

Rehfeld, K., Marwan, N., Breitenbach, S. F. M., and Kurths, J., 2013. Late Holocene Asian summer monsoon dynamics from small but complex networks of paleoclimate data, Clim. Dynam. 41, 3–19, doi:10.1007/s00382-012-1448-3.

Rhodes, E.J., 2011. Optically stimulated luminescence dating of sediments over the past 200,000 years. Annu. Rev. Earth Planet. Sci. 39, 461-488.

Roberts, R.G., Galbraith, R.F., Olley, J.M., Yoshida, H., Laslett, G.M., 1999. Optical dating of single and multiple grains of quartz from Jinmium rock shelter, northern Australia: part II, results and implications. Archaeometry 41 (2), 365-395.

Rugel, G., Pavetich, S., Akhmadaliev, S., Enamorado Baez, S.M., Scharf, A., Ziegenrücker, R., Merchel, S., 2016. The first four years of the AMS-facility DREAMS: Status and developments for more accurate radionuclide data, Nucl. Instr. Meth. Phys. Res. B 370, 94–100.

Ryavec, K.E., 2015. A historical atlas of Tibet. University of Chicago Press.

Schaefer, J.M., Oberholzer, P., Zhao, Z., Ivy-Ochs, S., Wieler, R., Baur, H., Kubik, P.W. and Schlüchter, C., 2008. Cosmogenic beryllium-10 and neon-21 dating of late Pleistocene glaciations in Nyalam, monsoonal Himalayas. Quaternary Science Reviews 27, 295-311.

Shen, C., Liu, K.-B., Morrill, C., Overpeck, J.T., Peng, J. and Tang, L., 2008. Ecotone shift and major droughts during the mid to late Holocene in the central Tibetan plateau. Ecology 89, 1079-1088.

Shi, X., Kirby, E., Furlong, K.P., Meng, K., Robinson, R., Lu, H. and Wang, E., 2017. Rapid and punctuated Late Holocene recession of Siling Co, central Tibet. Quaternary Science Reviews 172, 15-31.

Shi, Y. and Li, J., 1981. Glaciological research of the Qinghai-Xizang Plateau in China: Proceedings of Symposium on Qinghai-Xizang (Tibet) Pletau (Beijing, China), V. II, p. 1589-1597.

Sinha, A., Stott, L., Berkelhammer, M., Cheng, H., Edwards, R.L., Buckley, B., Aldenderfer, M. and Mudelsee, M., 2011. A global context for megadroughts in monsoon Asia during the past millennium. Quaternary Science Reviews 30, 47-62.

Sinha, A., Stott, L., Berkelhammer, M., Cheng, H., Edwards, R.L., Buckley, B., Aldenderfer, M. and Mudelsee, M., 2011. A global context for megadroughts in monsoon Asia during the past millennium. Quaternary Science Reviews 30, 47-62.

Staubwasser, M., Sirocko, F., Grootes, P. M., & Segl, M., 2003. Climate change at the 4.2 ka BP termination of the Indus valley civilization and Holocene south Asian monsoon variability. Geophysical Research Letters 30(8).

Stauch, G., 2015. Geomorphological and palaeoclimate dynamics recorded by the formation of aeolian archives on the Tibetan Plateau. Earth-Science Reviews 150, 393-408.

Stoffel, M., Bollschweiler, M., & Beniston, M., 2011. Rainfall characteristics for periglacial debris flows in the Swiss Alps: past incidences–potential future evolutions. Climatic Change 105, 263-280.

Stone J.O., 2000. Air pressure and cosmogenic isotope production. Journal of Geophysical Research: Solid Earth 105: 23753–23759.

Stone, J.O., 2000. Air pressure and cosmogenic isotope production. Journal of Geophysical Research: Solid Earth, 105(B10), 23753-23759.

Stuiver, M., Polach, H. A., 1977. Discussion: Reporting of ^{14}C data. Radiocarbon 19, 355–363. doi:10.1017/S0033822200003672

Sun, J., Li, S., Muhs, D.R., Li, B., 2007. Loess sedimentation in Tibet: provenance, processes, and link with Quaternary glaciations. Quat. Sci. Rev. 26, 2265–2280.

Taylor, M., Yin, A., Ryerson, F., Kapp, P., and Ding, L. 2003. Conjugate strike slip faulting along the Bangong–Nujiang suture zone accommodates coeval east–west extension and north-south shortening in the interior of the Tibetan plateau. Tectonics 22:2044.

Tian, L., Mstievenard, V.M.D., Yao, T., and Jouzel, J., 2001. Tibetan Plateau summer monsoon northward extent revealed by measurements of water stable isotopes: Journal of Geophysical Research 106(D22), 28081-28088, doi: 10.1029/2001JD900186.

Vandenberghe, J., 2002. The relation between climate and river processes. landforms and deposits during the Quaternary. Quaternary International 91, 17-23.

Vandenberghe, J., 2003. Climate forcing of fluvial system development: an evolution of ideas. Quaternary Science Reviews 22, 2053-2060.

Vandenberghe, J., Renssen, H., van Huissteden, K., Nugteren, G., Konert, M., Lu, H., Dodonov, A. and Buylaert, J.-P., 2006. Penetration of Atlantic westerly winds into Central and East Asia. Quaternary Science Reviews 25, 2380-2389.

Vega, M.B. and Craig, N., 2009. New experimental data on the distance of sling projectiles. Journal of Archaeological Science 36, 1264-1268.

Vermeesch, P., 2007. CosmoCalc: An Excel add-in for cosmogenic nuclide calculations. Geochemistry, Geophysics, Geosystems 8. 8.

Wang, B. and French, H.M., 1995a. In-situ creep of frozen soil, Fenghuo Shan area, Tibetan Plateau, China. Candadian Geotechnical Journal 32, 545-552.

Wang, B., & French, H. M., 1995b. Permafrost on the

Tibet plateau, China. Quaternary Science Reviews 14, 255-274.

Wang, B.L. and French, H.M., 1995c. Implications of Frost Heave for Patterned-Ground, Tibet Plateau, China. Arctic and Alpine Research 27, 337-344.

Wang, Y., Cheng, H., Edwards, R.L., Kong, X., Shao, X., Chen, S., Wu, J., Jiang, X., Wang, X. and An, Z., 2008. Millennial- and orbital-scale changes in the East Asian monsoon over the past 224,000 years. Nature 451, 1090-1093.

Weiwen, H., 1994. The pehistoric human occupation of the Qinghai-Xizang (Tibet) Plateau. Göttinger Geographische Schriften 95, 201-219.

Wilson, A.D., Zhu, Q., Barham, L., Stanistreet, I. and Bingham, G.P., 2016. A Dynamical Analysis of the Suitability of Prehistoric Spheroids from the Cave of Hearths as Thrown Projectiles. Scientific Reports 6, 30614

Wintle, A.G., 1997. Luminescence dating: laboratory procedures and protocols. Radiat. Meas. 27 (5), 760-817.

Wünnemann, B., Demske, D., Tarasov, P., Kotlia, B.S., Reinhardt, C., Bloemendal, J., Diekmann, B., Hartmann, K., Krois, J., Riedel, F. and Arya, N., 2010. Hydrological evolution during the last 15kyr in the Tso Kar lake basin (Ladakh, India), derived from geomorphological, sedimentological and palynological records. Quaternary Science Reviews 29, 1138-1155.

Xu, X. and Yi, C., 2014. Little Ice Age on the Tibetan Plateau and its bordering mountains: evidence from moraine chronologies. Global and Planetary Change 116, 41-53.

Xu, Z.X., Gong, T.L. and Li, J.Y., 2008. Decadal trend of climate in the Tibetan Plateau—regional temperature and precipitation. Hydrological Processes: An International Journal, 22(16), pp.3056-3065.

Yadava, A.K., Bräuning, A., Singh, J. and Yadav, R.R., 2016. Boreal spring precipitation variability in the cold arid western Himalaya during the last millennium, regional linkages, and socio-economic implications. Quaternary Science Reviews 144, 28-43.

Yan, D., Wünnemann, B., Zhang, Y., Long, H., Stauch, G., Sun, Q. and Cao, G., 2018. Response of lake-catchment processes to Holocene climate variability: Evidences from the NE Tibetan Plateau. Quaternary Science Reviews 201, 261-279.

Yao, T., Masson-Delmotte, V., Gao, J., Yu, W., Yang, X., Risi, C., Sturm, C., Werner, M., Zhao, H., He, Y. and Ren, W., 2013. A review of climatic controls on δ18O in precipitation over the Tibetan Plateau: Observations and simulations. Reviews of Geophysics 51, 525-548.

Ye, Q., Bolch, T., Naruse, R., Wang, Y., Zong, J., Wang, Z., Zhao, R., Yang, D. & Kang, S., 2015. lacier mass changes in Rongbuk catchment on Mt. Qomolangma from 1974 to 2006 based on topographic maps and ALOS 20 PRISM data. Journal of Hydrology 530, 273-280.

You, Q., Kang, S., Pepin, N., Flügel, W.A., Yan, Y., Behrawan, H. and Huang, J., 2010. Relationship between temperature trend magnitude, elevation and mean temperature in the Tibetan Plateau from homogenized surface stations and reanalysis data. Global and Planetary Change 71, 124-133.

Youwu, Zhou, and Guo Dongxin, 1982. Principal characteristics of permafrost in China. Journal of Glaciology and Geocryology 4, 1-19 (in Chinese)

Yu, L., Lai, Z., 2014. Holocene climate change inferred from stratigraphy and OSL chronology of aeolian sediments in the Qaidam Basin, northeastern Qinghai–Tibetan Plateau. Quat. Res. 81, 488–499.

Yu, W., Yao, T., Tian, L., Ma, Y., Ichiyanagi, K., Wang, Y., and Sun, W., 2008. Relationships between δ18O in precipitation and air temperature and moisture origin on a south-north transect of the Tibetan Plateau: Atmospheric Research 87, 158–169, doi: 10.1016/j.atmosres.2007.08.004.

Zech, R., Glaser, B., Sosin, P., Kubik, P.W. and Zech, W., 2005. Evidence for long-lasting landform surface instability on hummocky moraines in the Pamir Mountains (Tajikistan) from ^{10}Be surface exposure dating. Earth and Planetary Science Letters 237, 453-461.

Zhang Shenshui, 1976. New discovery of Palelithic from Dingri, Biet. In Chinese Academy of Sciences Multi-disciplinary Expedition of Quomolongma (Mt. Everest) 1966-1968, Sciences Press, Beijing, 105-109. (in Chinese)

Zhang, Qinghai, 2012. The lower Paleogene shallow-water limestones in the Tethyan Himalaya of Tibet and their implications for larger foraminiferal evolution, India-Asia collision and PETM-CIE." Unpublished PhD thesis, Staats-und Universitätsbibliothek Bremen,.

Zhou, H., Zhao, X., Tang, Y., Gu, S. and Zhou, L., 2005. Alpine grassland degradation and its control in the source region of the Yangtze and Yellow Rivers, China. Grassland Science 51, 191-203.

Zhou, Y. and Guo, D., 1982. Principal characteristics of permafrost in China (in Chinese). Journal of Glaciology and Geocryology 4, 1-19.

Zhu, L., Lü, X., Wang, J., Peng, P., Kasper, T., Daut, G., Haberzettl, T., Frenzel, P., Li, Q., Yang, R., Schwalb, A. and Mäusbacher, R., 2015. Climate change on the Tibetan Plateau in response to shifting atmospheric circulation since the LGM. Nature Scientific Reports 5, p. 13318.

Pratt-Sitaula, B., Burbank, D.W., Heimsath, A. and Ojha, T., 2004. Landscape disequilibrium on 1000–10,000 year scales Marsyandi River, Nepal, central Himalaya. Geomorphology, 58, 223-241.

Rixhon, G., Braucher, R., Bourlès, D., Siame, L., Bovy, B. and Demoulin, A., 2011. Quaternary river incision in NE Ardennes (Belgium)–Insights from 10Be/26Al dating of river terraces. Quaternary Geochronology, 6, 273-284.

Supplementary online information (SOM)

Meyer et al. *"Landscape dynamics and human-environment interactions in the northern foothills of Cho Oyu and Mount Everest (Tibet) during the Late Pleistocene and Holocene"*

	TIN 9 (periglacial)	**TIN 12 (aeolian)**	**TIN 14 (fluvial)**	**TIN 19 (aeolian)**
Zirkon (%)	4.2	9.8	5.4	11.1
Tourmaline (%)	15.2	18.7	18.6	17.3
Rutile (%)	0.3	0.3	0.9	0.6
Garnet (%)	19.1	16.9	17.2	14.8
Apatite (%)	17.9	13.8	23.1	13
Hornblende (%)	1.2	0.9	0	0
Kyanite (%)	40.9	39.3	34.5	43.2
Epidote (%)	1.2	0.3	0.3	0
Total number of grains (n)	335	326	333	162

SOM 1: Transparent heavy minerals extracted from sediment samples TIN 9, 12, 14 and 19 as percentage values and total number of counted grains (n). The samples are identical to the OSL samples TIN 9, 12, 14 and 19 (compare Figure 4 and text for stratigraphic position and sedimentary context). The heavy mineral assemblages are characterized by a high degree of similarity between each other, suggestive of a common source area for each sediment sample. Each sample further contained large amounts of muscovite, some biotite as well as opaque mineral grains, occasionally titanite and carbonate. The tourmaline grains are brownish or green-brown and rarely steel-blue in colour; the garnet grains are pinkish; the kyanite grains are partly rounded. Note that kyanite and garnet form during high grade metamorphism and both occur in relatively high abundance in our dataset. Such grains can still be sourced from the un-metamorphosed sandstone units of the Tibetan Sedimentary Sequence (as implied in the main text), because these sandstones can easily contain detrital grains from high-grade metamorphic rocks of previous orogenesis. This interpretation is in line with the observation that many of the kyanite grains are rounded.

Inventory number	Morphologic features	Status	Altitude m asl.	Exposure	Latitude	Longitude
002	distinct steep snout	intact	5471	N	28°19'47.79"N	87° 4'51.61"E
028	distinct steep snout	intact	5146	N	28°28'32.95"N	87°12'50.07"E
027	distinct steep snout	intact	5052	NW	28°28'45.02"N	87°12'45.96"E
025	distinct steep snout	intact	5050	N	28°29'7.30"N	87°13'8.43"E
026	distinct steep snout	intact	4981	W	28°29'5.97"N	87°12'54.60"E
009	distinct steep snout	intact	4980	N	28°29'46.86"N	87°12'17.08"E
010	distinct steep snout	intact	4945	N	28°29'48.72"N	87°12'13.73"E
006	distinct steep snout	intact	4934	NW	28°30'9.74"N	87°13'0.33"E
008	distinct steep snout	intact	4920	N	28°29'54.83"N	87°12'27.08"E
017	distinct steep snout	intact	4905	W	28°28'53.17"N	87°11'27.37"E
011	distinct steep snout	intact	4900	N	28°29'45.43"N	87°11'59.72"E
018	distinct steep snout	intact	4870	W	28°28'49.61"N	87°11'19.12"E
	intact rock glaciers median altitude (± standard deviation)		*4963*	*164*		
007	strongly incised	relict	4808	S	28°30'4.06"N	87°12'33.37"E
014	partly incised	relict	4777	N	28°29'9.41"N	87°11'57.46"E
019	partly incised	relict	4596	W	28°28'53.34"N	87°10'54.06"E
022	sparsely vegetated & incised	relict	4560	N	28°25'33.84"N	87°12'52.11"E
023	sparsely vegetated & incised	relict	4538	N	28°25'34.55"N	87°12'35.87"E
020	partly incised	relict	4450	W	28°28'47.57"N	87°10'22.59"E
	relict rock glaciers median altitude (± standard deviation)		4578	141		

SOM 2: A sample of rock glaciers from the wider Su-re area. The altitudinal position of the individual rock glacier fronts are indicated as well as the average altitude for each group (i.e. intact rock glaciers that are likely containing ice; relict rock glaciers likely to contain no ice).

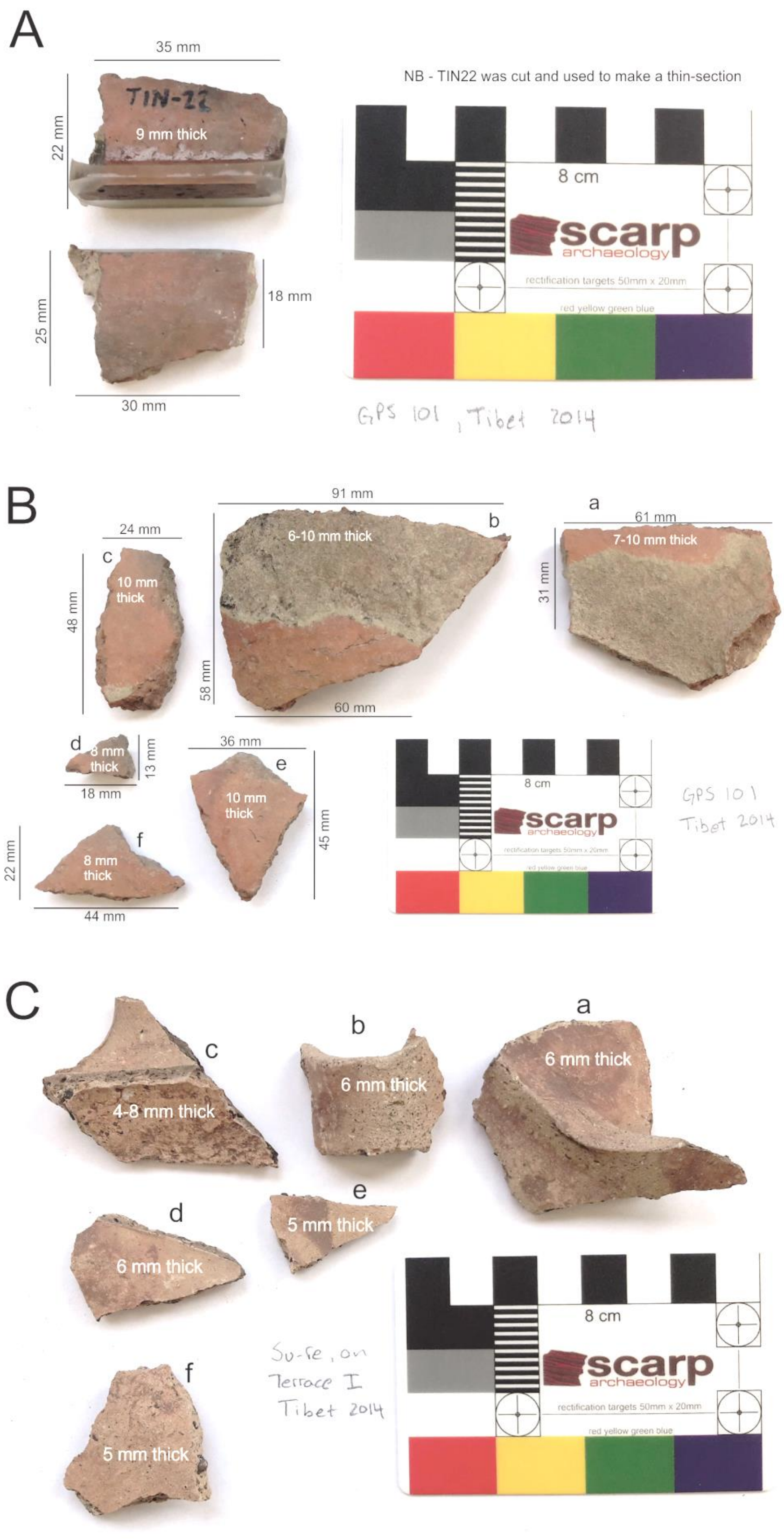

SOM 3: Ceramic sherds from Su-re; samples C 22 (A), C 23 (B) and C 28 (C). See figure 4 for their stratigraphic positions. Sample C 28 is a surface sample from terrace 2. See text for details.

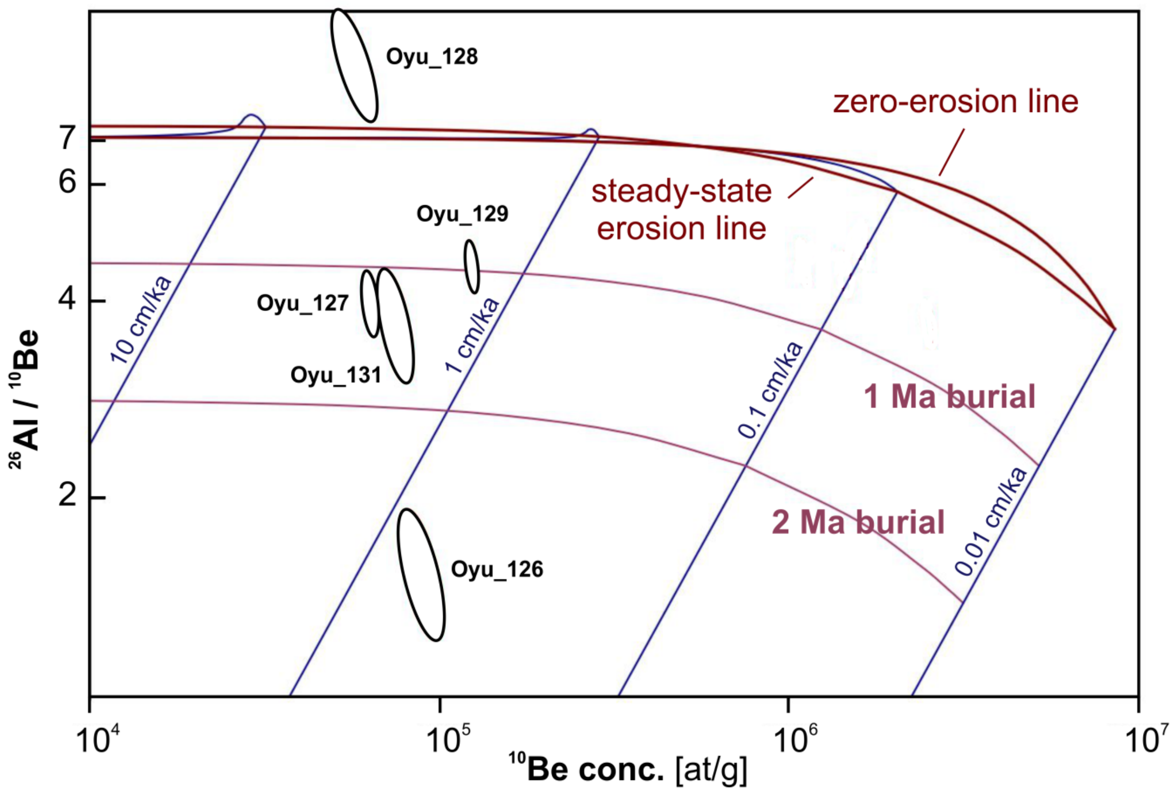

SOM 4: ^{10}Be concentrations plotted against ^{26}Al/^{10}Be concentrations for the five Cho Oyu samples investigated in this study (so called 'banana plot').